J. Fluid Mech. (1968), *vol.* 32, *part* 4, *pp.* 737–764
Printed in Great Britain

On source–sink flows in a rotating fluid

By R. HIDE†

Department of Geology and Geophysics and Department of Physics,
Massachusetts Institute of Technology, Cambridge, Massachusetts 02139, U.S.A.

(Received 22 June 1967 and in revised form 11 December 1967)

An incompressible fluid fills a container of fixed shape and size and of uniform cross-section in the (x, y)-plane, the m rigid side walls and the two rigid end walls being in contact with the fluid. Here (x, y, z) are the Cartesian co-ordinates of a general point in the frame of reference in which the container is stationary. Fluid is withdrawn from the container at Q cm^3/sec via certain permeable parts of the side walls and replaced at the same steady rate via other permeable parts of the side walls. As, by hypothesis, the vorticity of the entering and leaving fluid relative to the container is zero, the concomitant fluid motion within the container, Eulerian velocity $\mathbf{u} = -\nabla\phi - \nabla \times \mathbf{A}$, is irrotational when the container is stationary in an inertial frame. The present paper is concerned with the effects on $\mathbf{u}$ of uniform rotation of the whole system with angular velocity $\mathbf{\Omega}$ about the z-axis when the normal component of $\mathbf{u}$ on the side walls is independent of z.

In the simplest conceivable case, $D \equiv z_u - z_l$ is infinite (but D/Q remains finite). End effects are then negligible and $\mathbf{u}$ is everywhere independent of z. The solenoidal component of $\mathbf{u}$, $-\nabla \times \mathbf{A}$, corresponds to j gyres, one for each of the j irreducible sets of circuits across which the net flow of fluid does not vanish that can be drawn within the m-ply connected region bounded by the side walls. While $\nabla\phi$, which satisfies $\nabla^2\phi = 0$, depends on Q but not on Ω, j and ν (the coefficient of kinematic viscosity), $\nabla \times \mathbf{A}$ depends on all these quantities but vanishes identically when $j\Omega = 0$. When $j\Omega \neq 0$ but $\nu \to 0$, $\nabla^2\mathbf{A} + 2\mathbf{\Omega}$, the absolute vorticity, tends to zero everywhere except in certain singular regions near the bounding surfaces, where boundary layers form.

End effects cannot be ignored when D is finite. When D is independent of x and y and equal to D_0 (say) and Ω is sufficiently large for the boundary layers on the end walls to be of the Ekman type, 95% thickness $\delta = 3(\nu/\Omega)^{\frac{1}{2}}$ ($\delta \ll D_0$), the end effects that then arise are only confined to these boundary layers when $j = 0$. When $j \neq 0$ boundary-layer suction influences the flow everywhere; thus $\nabla^2\mathbf{A}$ and $\nabla\phi$ (but not $\nabla \times \mathbf{A}$) are reduced to zero in the main body of the fluid, the regions of non-zero $\nabla\phi$ and $\nabla^2\mathbf{A}$ being the Ekman boundary layers on the end walls and boundary layers of another type, 95 % thickness Δ_s (typically greater than δ), on the side walls. A theoretical analysis of the structure of these boundary layers shows that non-linear effects, though unimportant in the end-wall boundary layers, can be significant and even dominant in the side-wall boundary layers. The analysis of an axisymmetric system, whose side walls

† Now at the Meteorological Office, Bracknell, Berkshire, England.

are two coaxial cylinders, suggests an approximate expression for Δ_s. When D is not everywhere independent of x and y, *non*-viscous end effects arise which produce relative vorticity in the main body of the fluid even when $j = 0$.

Experiments using a variety of source–sink distributions generally confirm the results of the theory, show that instabilities of various kinds may occur under certain circumstances, and suggest several promising lines for future work.

1. Introduction

The work described in this paper began when I became interested in flows produced by various distributions of fluid sources and sinks in a rapidly rotating spherical shell of an incompressible fluid. I decided to investigate first a system that possesses many of the dynamical features of a spherical shell but is simpler to construct. The rigid container of the fluid was a right circular cylinder with a flat top and a conical base, and rotated about a vertical axis. One source and one sink were used, each shaped (effectively) like a long thin cylinder parallel to the axis of rotation. They were first placed at equal distances from that axis along a diameter of the cylindrical container, and later in other positions. The flows produced were striking and spectacular and conformed with general expectations based on Proudman's theorem (Proudman 1916) and the theory of the divergent Ekman layer (see Charney & Eliassen 1949; Prandtl 1952), but I soon realized that their detailed interpretation and the extension of the experiments to more complicated systems would require, in the first instance, a fairly thorough understanding of simpler systems. It was with this goal in mind that the present investigation was undertaken.

The conical base of the fluid container was replaced with a flat base. The flows that then occurred admitted of relatively straightforward interpretation, which pointed to the need to understand the vertical boundary layers on the surfaces of the sources and sinks. Although pertinent observations of these boundary layers were made, it became clear that their further study would be facilitated by changing to an annular arrangement, in which the source and the sink were coaxial cylinders. A fairly detailed study of annular systems was then carried out.

2. Scope of the present work

This paper comprises two main parts, a theoretical discussion followed by an account of the experiments. The theoretical discussion is pivoted about the properties of flows that are everywhere two-dimensional in planes perpendicular to the axis of rotation, but it is also necessary to consider in detail the effects on these two-dimensional flows of rigid walls at the axial extremities of the fluid. As a theoretical preliminary to the experiments, it is sufficient in this discussion of end effects to restrict attention to cases where the rate of rotation is so rapid that the end-wall boundary layers are of the Ekman type (Prandtl 1952), characterized by a balance between Coriolis and viscous forces. In dealing

with the *side*-wall boundary layers, however, it will be necessary to extend the theory of Stewartson-type boundary layers (Stewartson 1957) to cases where the non-linear terms in the equations of motion are important.

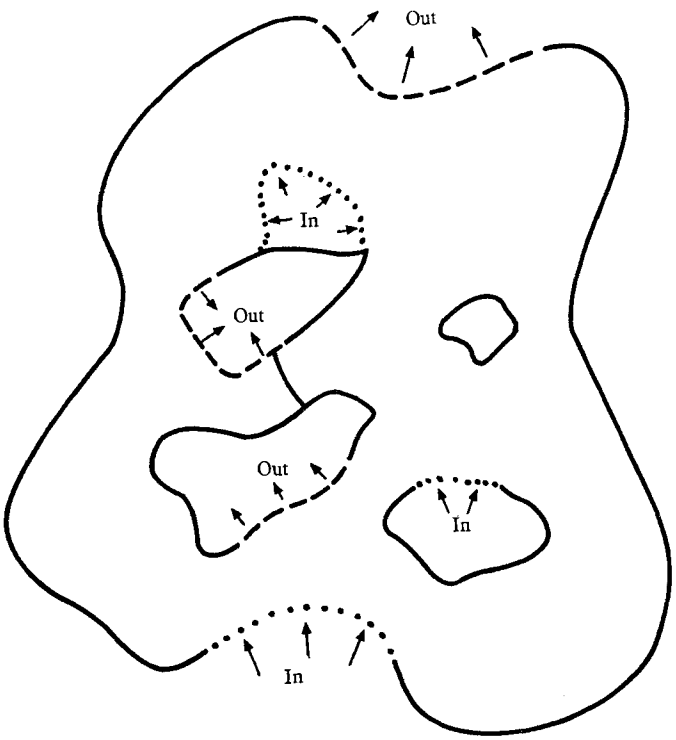

FIGURE 1. A general distribution of sources and sinks in a cylindrical container with m side walls $g_s(x, y) = 0$, $s = 1, 2, \ldots, m$ (where $m = 4$). Impermeable surfaces are indicated by full lines and permeable surfaces by dotted lines when the surface is a source, and dashed lines when the surface is a sink (cf. figures 3 and 4).

Theory

The theoretical discussion (§§ 3–5) may be summarized as follows. An incompressible fluid fills a container of fixed shape and size and of uniform cross-section in the (x, y)-plane, the surfaces occupied by the m rigid side walls, as illustrated in figure 1, and the two rigid end walls being $g_s(x, y) = 0$, $s = 1, 2, \ldots, m$, $z = z_u(x, y)$ and $z = z_l(x, y)$, $z_u > z_l$, respectively. Here (x, y, z) are the Cartesian co-ordinates of a general point in the frame of reference in which the container is stationary. Fluid is withdrawn from the container at Q cm^3/sec via certain permeable parts of the side walls and replaced at the same rate via other permeable parts of the side walls.

By hypothesis, the entering fluid has zero vorticity relative to the container. Consequently, when the container is stationary in an inertial frame of reference the ensuing relative hydrodynamical motion of the fluid within the container is irrotational. That is to say the Eulerian velocity, $\mathbf{u}$, though in general expressible as

$$\mathbf{u} = -\nabla\phi - \nabla \times \mathbf{A}, \tag{2.1}$$

is then such that $-\nabla \times \mathbf{A}$, the solenoidal component of $\mathbf{u}$, is zero. ϕ is completely determined by the continuity equation,

$$\operatorname{div} \mathbf{u} = 0 = -\nabla^2 \phi, \tag{2.2}$$

solved under the boundary conditions that $\mathbf{u} \cdot \mathbf{n}$ is a specified function f at each point P of the walls of the container, where $\mathbf{n}$ is the outward-drawn normal at P.

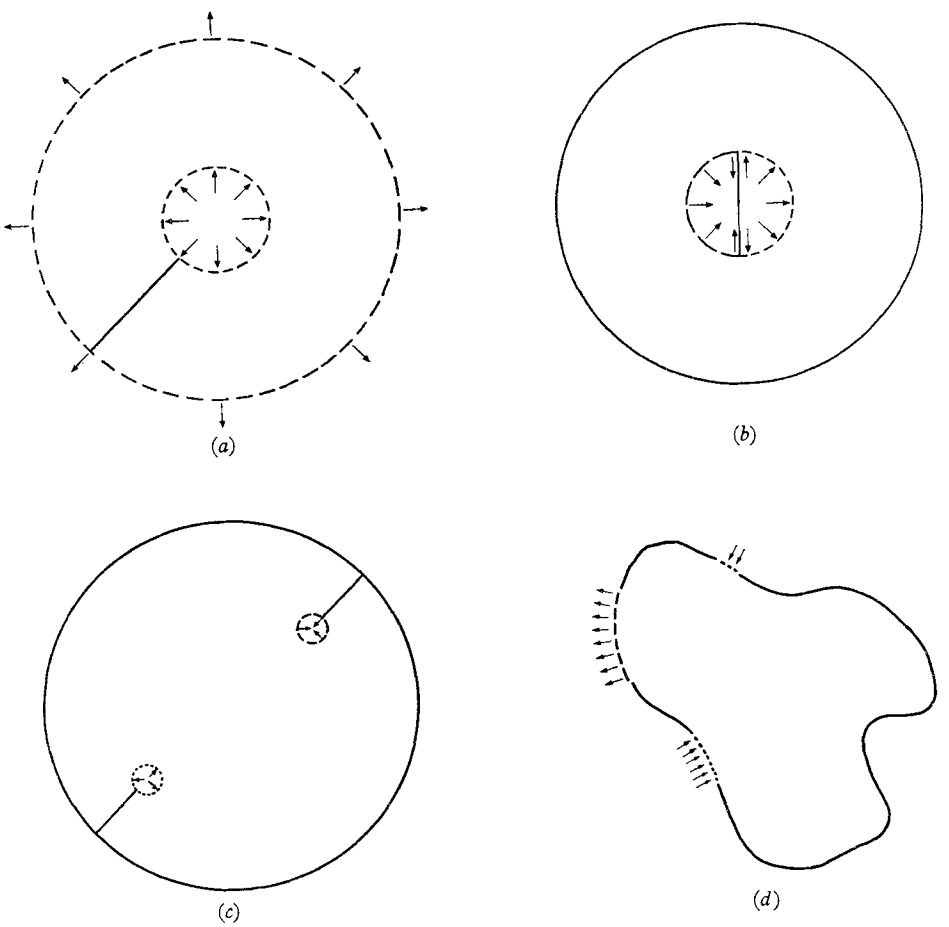

FIGURE 2. Examples of distributions of sources and sinks for which j, the number of irreducible sets of closed curves across which the net flow of fluid does not vanish, is zero (see (3.16) and (3.17)). (*a*), (*b*) and (*c*) represent the key to the distributions used in the experiments illustrated in figure 6 (see table 1); (*d*) is any simply connected region (i.e. $m = 1$, cf. figure 1).

When the container is not stationary in an inertial frame, $-\nabla \times \mathbf{A}$ is no longer in general equal to zero. If the apparatus rotates with uniform angular velocity $\boldsymbol{\Omega}$ about the z-axis, then the equation of motion is

$$\partial \mathbf{u}/\partial t + (\mathbf{u} \cdot \nabla)\,\mathbf{u} + 2\boldsymbol{\Omega} \times \mathbf{u} = -\nabla p + \nu \nabla^2 \mathbf{u}, \tag{2.3}$$

where t denotes time, p is the total kinematic pressure (i.e. pressure divided by density) minus the potential of gravitational and centripetal force per unit mass,

and ν is the coefficient of kinematic viscosity. Take the *curl* of (2.3), and, on making use of (2.1) and (2.2), we find for the relative vorticity,

$$\boldsymbol{\omega} \equiv \nabla \times \mathbf{u} = \nabla^2 \mathbf{A}, \tag{2.4}$$

the following equation:

$$\partial \boldsymbol{\omega}/\partial t + (\mathbf{u} \,.\, \nabla)\, \boldsymbol{\omega} - \nu \nabla^2 \boldsymbol{\omega} - (\boldsymbol{\omega} \,.\, \nabla)\, \mathbf{u} - 2\Omega\, \partial \mathbf{u}/\partial z = -(2\Omega + \boldsymbol{\omega}) \operatorname{div} \mathbf{u} = 0. \tag{2.5}$$

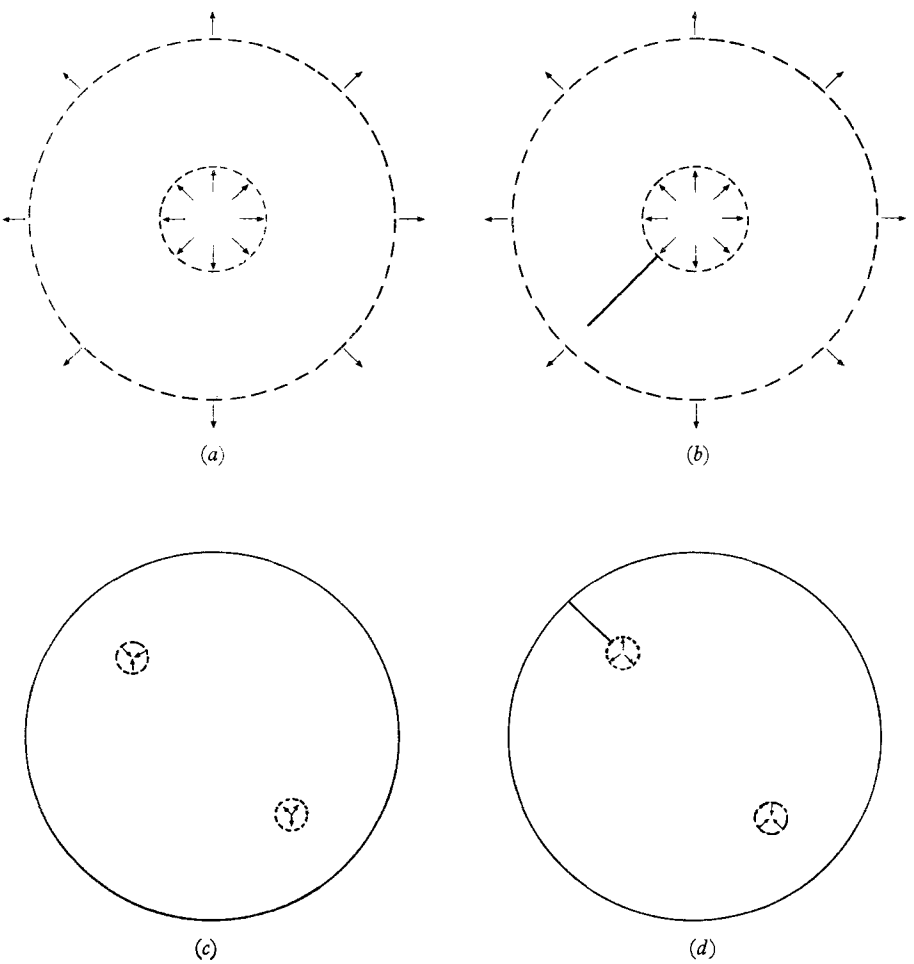

FIGURE 3. Examples of distributions of sources and sinks for which $j \neq 0$ (see (3.16) and (3.17)). They represent the key to the distributions used in the experiments illustrated in figure 7 (see table 1, also figures 8, 9, 10, 12 and 13). $m = 2$, $j' = 2$ and $j = 1$ for (*a*), (*b*) and (*d*); $m = 3$, $j' = 2$, $j = 2$ for (*c*) (see (3.11) and (3.12)).

$\boldsymbol{\omega} = 0$ satisfies (2.5) when $\Omega\, \partial \mathbf{u}/\partial z = 0$, so that when $\Omega \neq 0$, $\mathbf{u}$ is only irrotational when $\partial \mathbf{u}/\partial z = 0$ and the boundary conditions are independent of Ω (see Taylor 1917). Otherwise $\boldsymbol{\omega} \neq 0$ in general when $\Omega \neq 0$.

Strictly two-dimensional flows (i.e. $\partial \mathbf{u}/\partial z = 0$) are treated in §3. Such flows arise when f is independent of z and

$$D \equiv z_u - z_l \tag{2.6}$$

is infinite (but Q/D remains non-zero), so that end effects are negligible. It is shown that the solenoidal component of $\mathbf{u}$ corresponds to j gyres, one for each of the j irreducible sets of closed curves that can be drawn within the m-ply connected region bounded by $g_s(x,y) = 0$, $s = 1, 2, \ldots, m$ (the cross-section of the container in the (x,y)-plane, see figures 1–3) across which the net flow of fluid does not vanish. It follows, therefore, that $\nabla \times \mathbf{A} = 0$ everywhere in the special case $j = 0$ (see figure 2).

While $\nabla\phi$ is the same as in the non-rotating case, $\nabla \times \mathbf{A}$ depends on Ω as well as on Q, and when ν tends to zero and the flow is steady (and $j \neq 0$),

$$\boldsymbol{\omega} \equiv \nabla^2\mathbf{A} = \left(0, 0, \frac{\partial^2 A_z}{\partial x^2} + \frac{\partial^2 A_z}{\partial y^2}\right) = (0, 0, -2\Omega) \tag{2.7a}$$

and

$$\nabla(p + \tfrac{1}{2}\mathbf{u}.\mathbf{u}) = 0 \tag{2.7b}$$

within the main body of the fluid, but not in certain singular regions, where boundary layers form. (An exact solution for steady, axisymmetric (but $\nu \neq 0$) flow is given in the appendix.) In the special case $j = 0$, in place of (2.7) we have

$$\nabla^2\mathbf{A} = \nabla \times \mathbf{A} = 0 \quad \text{and} \quad \nabla(p + \tfrac{1}{2}\mathbf{u}.\mathbf{u}) + 2\boldsymbol{\Omega} \times \mathbf{u} = 0. \tag{2.8a,b}$$

End effects can be very important in practice, and it is necessary, therefore, to examine in §§4 and 5 the theory of such effects on the strictly two-dimensional flows discussed in §3. Purely *viscous* end effects arise when D is finite but independent of x and y and then equal to D_o, say. It is assumed for convenience that Ω is so large that the viscous boundary layers on the end walls are of the Ekman type, 95 % thickness

$$\delta \equiv 3(\nu/\Omega)^{\frac{1}{2}} \tag{2.9}$$

(see Prandtl 1952). Only when $j = 0$ are viscous end effects confined to these Ekman layers. Otherwise, when $j \neq 0$, Ekman-layer suction exerts a radical influence on the flow everywhere. Thus $\nabla^2\mathbf{A}$ and $\nabla\phi$ (but not $\nabla \times \mathbf{A}$) are reduced to zero in the main body of the fluid, the regions of non-zero $\nabla\phi$ and $\nabla^2\mathbf{A}$ being the Ekman boundary layers on the end walls and boundary layers of another type, 95 % thickness Δ_s, that then occur on the side walls.

A theoretical analysis of the structure of these boundary layers is presented in §5, where it is shown that non-linear effects, though unimportant in the Ekman layers, can be significant and even dominant in the side-wall boundary layers. The analysis of an axisymmetric system, whose side walls are two coaxial cylinders, suggests that

$$\Delta_s \doteqdot \sqrt{3}\,\delta^{\frac{1}{2}} D_o^{\frac{1}{2}}[(1 + \tfrac{1}{4}X_s^2)^{\frac{1}{2}} \pm \tfrac{1}{2}X_s]/\sqrt{2}, \tag{2.10}$$

taking the upper sign for the boundary layer on the cylinder via which the fluid enters the container, the source, and the lower sign for the boundary layer on the other cylinder, the sink, where

$$X_s \equiv Q_s/3\sqrt{2}\,L_s D_o^{\frac{1}{2}} \nu^{\frac{3}{4}} \Omega^{\frac{1}{4}}, \tag{2.11}$$

a dimensionless parameter, L_s being the perimeter of the side wall and Q_o the rate of transfer of fluid across it. Thus

$$\Delta_s \doteqdot 3\nu^{\frac{1}{4}} D_o^{\frac{1}{2}}/\sqrt{2}\,\Omega^{\frac{1}{4}} \text{ (source and sink)} \quad \text{when} \quad X_s \ll 1 \tag{2.12a}$$

but

$$\Delta_s \doteqdot Q/2L_s\nu^{\frac{1}{2}}\Omega^{\frac{1}{2}} \text{ (source)}, \quad \Delta_s \doteqdot 9DL_s\nu/Q_o \text{ (sink)} \quad \text{when} \quad X_s \gg 1. \quad (2.12b)$$

In contrast to the case of constant D, *non*-viscous end effects arise when D is not independent of x and y; and when the range of variation of D greatly exceeds $(\nu/\Omega)^{\frac{1}{2}}$, *viscous* end effects are negligible in comparison. Of particular interest is the case $j = 0$; $\nabla \times \mathbf{A}$ and $\nabla^2\mathbf{A}$ no longer vanish when non-viscous end effects are present.

Experiments

The experimental part of the paper begins with a brief discussion of apparatus and techniques (§6). This is followed by accounts of experiments with systems subject first to viscous end effects (§7) and then to non-viscous end effects (§8), using various distributions of sources and sinks, notably those illustrated by figure 2, for which $j = 0$, and figure 3, for which $j \neq 0$. The experimental results are consistent with the theoretical predictions, show that instabilities of various kinds may occur under certain circumstances, and suggest several promising lines for future theoretical and experimental work.

3. Strictly two-dimensional flows

Let us first consider flows that are everywhere strictly two-dimensional in planes perpendicular to the rotation axis (i.e. $\partial\mathbf{u}/\partial z = \partial p/\partial z = 0$). Such flows occur when $f(P)$ (see (2.2)) is independent of z, and when D, the depth of the fluid, is infinite (but

$$q \equiv Q/D \quad (3.1)$$

is non-zero). We impose no restriction at this stage on the value of Ω.

In general, the boundary conditions are as follows:

$$\left.\begin{aligned} \nu(\mathbf{u}\times\mathbf{n}) = 0 \quad \text{on} \quad (a)\ g_s(x,y) = 0 \quad (s = 1,2,\ldots,m), \\ \text{and on} \quad (b)\ z = z_u(x,y) \quad \text{and} \quad z = z_l(x,y), \end{aligned}\right\} \quad (3.2a,b)$$

$$\mathbf{u}.\mathbf{n} = f(P) \quad \text{on} \quad g_s(x,y) = 0 \quad (s = 1,2,\ldots,j'), \quad (3.3a)$$

$$\mathbf{u}.\mathbf{n} = 0 \quad \text{on} \quad g_s(x,y) = 0 \quad (s = (j'+1),(j'+2),\ldots,m), \quad (3.3b)$$

and

$$\mathbf{u}.\mathbf{n} = 0 \quad \text{on} \quad z = z_u(x,y) \quad \text{and} \quad z = z_l(x,y), \quad (3.3c)$$

where $\mathbf{n}$ is the outward-drawn unit normal at the general point P on the side wall. Equations (3.2) express the requirement that the tangential component of $\mathbf{u}$ must vanish on a rigid surface (the 'no-slip' condition) when $\nu \neq 0$. Equations (3.3) state that the normal component of $\mathbf{u}$ must vanish on the completely impermeable side walls numbered $(j'+1)$ to m and on the impermeable end walls in $z = z_u$ and $z = z_l$, and that $\mathbf{u}.\mathbf{n}$ is a specified quantity $f(P)$ at each point on the other side walls, numbered 1 to j' (see figures 1–3).

Clearly $f(P)$ satisfies

$$\sum_{s=1}^{j'} \iint f(P)\,d\sigma = 0, \quad \sum_{s=1}^{j'} \iint |f(P)|\,d\sigma = 2Q, \quad (3.4)$$

where $d\sigma$ is an element of area at P and each integral is taken over the whole surface defined by $g_s(x, y) = 0$.

As we are dealing here with flows that are independent of z we can set the z component of $\mathbf{u}(= (u, v, w))$ and the x and y components of $\mathbf{A}(= (A_x, A_y, A_z))$ equal to zero, see (2.1). Equations (2.3), (2.2), (2.4) and (2.5) then reduce to

$$(\partial/\partial t - \nu\nabla_1^2)(\mathbf{k} \times \nabla_1 A_z) + (2\Omega + \nabla_1^2 A_z)(\nabla_1 \phi \times \mathbf{k} - \nabla_1 A_z) = -\nabla_1 p^*, \tag{3.5}$$

$$\nabla_1^2 \phi = 0, \tag{3.6}$$

$$\boldsymbol{\omega} \equiv (\xi, \eta, \zeta) = (0, 0, \nabla_1^2 A_z) \tag{3.7}$$

and

$$\left(\frac{\partial}{\partial t} + u\frac{\partial}{\partial x} + v\frac{\partial}{\partial y} - \nu\nabla_1^2\right)\nabla_1^2 A_z = 0, \tag{3.8}$$

where

$$p^* \equiv p + \tfrac{1}{2}(u^2 + v^2) + \partial\phi/\partial t \tag{3.9}$$

and

$$\nabla_1 \equiv \mathbf{i}\frac{\partial}{\partial x} + \mathbf{j}\frac{\partial}{\partial y} = \nabla - \mathbf{k}\frac{\partial}{\partial z}, \tag{3.10}$$

($\mathbf{i}$, $\mathbf{j}$, $\mathbf{k}$) being unit vectors parallel, respectively, to the x-, y- and z-axes. The boundary conditions (3.2) reduce to

$$\nu(\mathbf{u} \times \mathbf{n}) = 0 \quad \text{on} \quad g_s(x, y) = 0 \quad (s = 1, 2, \ldots, m) \tag{3.11}$$

and

$$\left.\begin{aligned} -\mathbf{n}.\nabla_1\phi &= f(P) \quad \text{on} \quad g_s(x, y) = 0 \quad (s = 1, 2, \ldots, j'), \\ -\mathbf{n}.\nabla_1\phi &= 0 \quad \text{on} \quad g_s(x, y) = 0 \quad (s = (j'+1), (j'+2), \ldots, m). \end{aligned}\right\} \tag{3.12}$$

When $\Omega = 0$, (3.5)–(3.12) are satisfied by

$$\nabla_1 A_z = 0, \quad (u, v) = -\nabla_1\phi, \quad \nabla_1 p^* = 0. \tag{3.13}$$

Equation (2.5) indicates that there may be circumstances in which $\mathbf{u}$ remains irrotational (i.e., $\nabla_1 A_z = 0$) even when $\Omega \neq 0$, and we now proceed to examine this point by setting $\nabla_1 A_z = 0$ in (3.5), which then reduces to

$$\nabla_1 p^* = 2\Omega\mathbf{k} \times \nabla_1\phi \quad (\text{when } \nabla_1 A_z = 0). \tag{3.14}$$

Take the line integral of equation (3.14) around any closed curve $\mathscr{C}$ that everywhere lies within the fluid and in the (x, y)-plane and find

$$\oint_{\mathscr{C}} \nabla_1 p^* . d\mathbf{c} = 2\Omega \oint_{\mathscr{C}} (\mathbf{k} \times \nabla_1\phi) . d\mathbf{c} \quad (\text{when } \nabla_1 A_z = 0), \tag{3.15}$$

where $d\mathbf{c}$ is an element of length of $\mathscr{C}$. As p^* and ϕ are single-valued functions of position it follows from (3.15) that

$$\nabla_1 A_z = 0 \quad \text{when} \quad 2\Omega\mathscr{F}_{\mathscr{C}} = 0 \quad \text{for all possible } \mathscr{C}, \tag{3.16}$$

where

$$\mathscr{F}_{\mathscr{C}} \equiv \oint (\mathbf{k} \times \nabla_1\phi) . d\mathbf{c} \tag{3.17}$$

(see Barcilon 1967; Hide 1966, 1967).

$\mathscr{F}_{\mathscr{C}}$ is the net flow of fluid across the closed curve $\mathscr{C}$. Denote by j the number of 'irreducible sets' (see Lamb 1945, p. 49) of such curves for which $\mathscr{F}_{\mathscr{C}} \neq 0$; it

follows from (3.16) that $\mathbf{k}\times\nabla_1 A_z$, the solenoidal component of $\mathbf{u}$ (see (2.1)), vanishes when $j = 0$, as in the cases illustrated by figure 2, but not when $j \neq 0$, as in the cases illustrated by figure 3.

j depends on the connectivity m of the cross-section of the container in the (x, y)-plane and on the form of $f(P)$; it is obvious that $j \leqslant j'$ (see (3.3)). $m = 1$, $j' = 1$ and $j = 0$ for figures $2a, c$ and d; $m = 2, j' = 1$ and $j = 0$ for figure $2b$; $m = 2$, $j' = 2$ and $j = 2$ for figure $3c$.

When $j \neq 0$, the source–sink potential flow interacts with the basic rotation to produce j gyres of non-zero relative vorticity, $\nabla_1^2 A_z$, one surrounding each bounding surface through which the net flow of fluid does not vanish.† Observe that when $\nu = 0$ and the flow is steady,

$$\nabla_1^2 A_z = -2\Omega, \quad \nabla_1 p^* = 0 \quad (j \neq 0); \tag{3.18}$$

the corresponding results when $j = 0$ are

$$\nabla_1 A_z = \nabla_1^2 A_z = 0, \quad \nabla_1 p^* = -2\Omega\mathbf{k}\times\nabla_1\phi \quad (j = 0) \tag{3.19}$$

(cf. (3.13), (3.14), (2.7) and (2.8) above, also (A 4) and (A 7) below).

When the flow is steady and axisymmetric (see figure $3a$), an exact solution to (3.5)–(3.12) can be readily obtained, even when $\nu \neq 0$. The case illustrated by figure $2a$ can also be treated with ease when ν is so small that its effects are confined to boundary layers on the radial connecting wall. These problems are considered in the appendix. There should be no difficulty involved in extending the analysis there presented to simple cases of non-axisymmetric flows, such as those due to source–sink arrangements given in figures $2b$, $2c$ and $3c$.

4. End effects

The extent to which the strictly two-dimensional flows discussed in § 3 would be expected to resemble the actual flows that occur when the depth, $D \equiv z_u - z_l$ (see (2.6)), of the container is finite depends on a number of factors, which we shall now consider.

The boundary conditions that $\mathbf{u} = 0$ on $z = z_u$ and $z = z_l$ must now be taken into account (see (3.2b) and (3.3c)). Suppose that viscous boundary layers of thickness d_u and d_l, both much less than D, occur on the end walls in $z = z_u$ and $z = z_l$, respectively. Also assume that the unit vectors normal to the end walls, respectively $\mathbf{n}_u$ and $\mathbf{n}_l$, where

$$\mathbf{n}_{u,l}(x, y) \equiv \nabla(z_{u,l}(x, y) - z)/|\nabla(z_{u,l}(x, y) - z)|, \tag{4.1}$$

make such small angles, $\cos^{-1}(\mathbf{k}.\mathbf{n}_{u,l})$, with the z-axis that second- and higher-order effects in these angles can be neglected. (In the experiments $\cos^{-1}(\mathbf{k}.\mathbf{n}_u)$ was always zero and $\cos^{-1}(\mathbf{k}.\mathbf{n}_l)$ was either zero or $\pm\pi/18$ radians ($\pm 10°$), see table 1.)

† When the fluid is not incompressible the term $2\Omega\nabla.\mathbf{u}$ in (2.5) ensures that $\nabla_1^2 A_z \neq 0$ even when $j = 0$. Dynamical effects of finite compressibility are usually negligible in laboratory experiments with rotating fluids, but they are certainly very important in hypersonically-rotating fluids, such as the atmospheres of the major planets and rapidly rotating stars (see Hide 1963).

By equation (2.5), ζ satisfies

$$\left[\frac{\partial}{\partial t}+(\mathbf{u}.\nabla)\right]\zeta-\nu\nabla^2\zeta=(2\Omega+\zeta)\frac{\partial w}{\partial z}+\left(\xi\frac{\partial w}{\partial x}+\eta\frac{\partial w}{\partial y}\right), \tag{4.2}$$

which only reduces to (3.8) when $\partial\mathbf{u}/\partial z=0$. Denote by

$$\bar{\mathbf{u}}=(\bar{u},\bar{v},\bar{w}) \quad \text{and} \quad \bar{\boldsymbol{\omega}}=(\bar{\xi},\bar{\eta},\bar{\zeta})$$

the values of $\mathbf{u}=(u,v,w)$ and $\boldsymbol{\omega}=(\xi,\eta,\zeta)$ just outside the end-wall boundary layers. At this stage we make use of the fact that in all but one of the experiments described below (see §§6–8) Ω was so large that

$$|\bar{\boldsymbol{\omega}}|\ll 2\Omega \quad \text{and} \quad \left|\frac{\partial\bar{\boldsymbol{\omega}}}{\partial t}\right|\ll 2\Omega\bar{\boldsymbol{\omega}} \tag{4.3a,b}$$

and we introduce the further assumptions, which can be justified *a posteriori*, that

$$\left|\bar{\xi}\frac{\partial\bar{w}}{\partial x}+\bar{\eta}\frac{\partial\bar{w}}{\partial y}\right|\ll\left|2\Omega\frac{\partial\bar{w}}{\partial z}\right|, \tag{4.4a}$$

$$\left|\bar{w}\frac{\partial\bar{\zeta}}{\partial z}\right|\ll\left|\bar{u}\frac{\partial\bar{\zeta}}{\partial x}+\bar{v}\frac{\partial\bar{\zeta}}{\partial y}\right| \tag{4.4b}$$

and that $\bar{u}$, $\bar{v}$ and $\partial\bar{w}/\partial z$ are independent of z, the last quantity being given by

$$\frac{\partial\bar{w}}{\partial z}=\{w(z=z_u-d_u)-w(z=z_l+d_l)\}/D(x,y). \tag{4.5}$$

When (4.3) are satisfied, the end-wall boundary layers are of the Ekman type in which the motion parallel to the wall varies from zero at the wall to 95 % of its value in the main body of the fluid at a distance $3(\nu/\Omega\mathbf{k}.\mathbf{n})^{\frac{1}{2}}$ cm from the wall. It is a straightforward application of the theory of the Ekman boundary layer (Prandtl 1952) and (4.1) to show that the term in curly brackets on the right-hand side of (4.5) is equal to $\bar{\mathbf{u}}.\nabla_1 D(x,y)-(\nu/\Omega)^{\frac{1}{2}}\bar{\zeta}$; hence, by (4.2) to (4.5), $\bar{\zeta}$ satisfies

$$\frac{\partial\bar{\zeta}}{\partial t}+\bar{u}\frac{\partial\bar{\zeta}}{\partial x}+\bar{v}\frac{\partial\bar{\zeta}}{\partial y}-\nu\nabla_1^2\bar{\zeta}\doteq\frac{2\Omega}{D(x,y)}\left[-\left(\frac{\nu}{\Omega}\right)^{\frac{1}{2}}\bar{\zeta}+\bar{\mathbf{u}}.\nabla_1 D(x,y)\right]. \tag{4.6}$$

We shall use this equation as a basis for the following discussion of end effects.

$\bar{u}$ and $\bar{v}$ can be regarded as the x- and y-components of velocity of a fluid filament at (x,y) that everywhere lies parallel to the z-axis, and $\bar{\zeta}$ is the z-component of vorticity of that filament. The right-hand side of (4.6) measures the rate of change of $\bar{\zeta}$ of a moving filament due to axial stretching of the filament. The viscous contribution to the stretching process, proportional to $(\nu/\Omega)^{\frac{1}{2}}\bar{\zeta}$, is due to Ekman boundary-layer suction; the non-viscous contribution, proportional to $\bar{\mathbf{u}}.\nabla_1 D(x,y)$, is due to variations of D with x and y.

When $j=0$ (see figure 2), the strictly two-dimensional flows discussed in §3 are irrotational (i.e. $\zeta=0$, see (3.16)). Such flows satisfy (4.6) automatically when D is constant (i.e. when $\nabla_1 D(x,y)=0$). Consequently end effects, which are then purely viscous, are confined to the Ekman layers and the flow elsewhere is unaffected by the presence of the end walls (cf. figure 6). At the other extreme, when $|\bar{\mathbf{u}}.\nabla_1 D(x,y)|\gg|(\nu/\Omega)^{\frac{1}{2}}\bar{\zeta}|$, the purely non-viscous end effects that

then arise affect the flow throughout the main body of the fluid. $\bar{\mathbf{u}}.\nabla_1 D(x,y)$ tends to zero nearly everywhere when (4.3) and (4.4) are satisfied, the corresponding filament trajectories being such that $D(x,y)$ remains constant along them (cf. figures 12*b*, *c*). Exceptional regions are concomitant side-wall boundary layers in which some of the other terms in (4.6) are non-zero, so that $\bar{\mathbf{u}}.\nabla_1 D(x,y)$ is also non-zero (cf. figures 12*b* and *c*). (The Gulf Stream and the low-level atmospheric jet stream off East Africa are probably geophysical examples of such boundary layers.)

In contrast to the case $j = 0$, when $j \neq 0$ (see figure 3) the strictly two-dimensional flows discussed in §3 are not irrotational (i.e. $\zeta \neq 0$, see (3.16)). By (4.6), therefore, the flow in the main body of the fluid is then influenced by viscous as well as non-viscous end effects. The ratio of the thickness of the end-wall boundary layer to the range of variation of $D(x,y)$ is a measure of the relative importance of viscous to non-viscous end effects; in what follows next we shall ignore the latter and consider only the former.

Figure 4 illustrates how purely viscous end effects can modify strictly two-dimensional flows when $j \neq 0$ (see also figure 3). Boundary-layer suction redistributes the irrotational and solenoidal components of $\mathbf{u}$ in a manner illustrated by figures 4*a* and 4*b* respectively.

The flow is best considered by splitting the meridional cross-section into five regions: the interior region, the two Ekman layers, the boundary layer on the surface of the source, and the boundary layer on the surface of the sink. The transfer of fluid from source to sink now takes place via these boundary layers, $\mathbf{u}$ in the interior region being such that

$$\left.\begin{aligned} w = 0, \quad \nabla_1\phi = 0, \quad \zeta \equiv \nabla_1^2 A_z = 0, \quad \frac{\partial}{\partial z}\nabla_1 A_z = 0, \\ \left(\frac{\nu}{\Omega}\right)^{\frac{1}{2}} \oint_{\mathscr{C}} (\mathbf{k}\times\nabla_1 A_z).d\mathbf{c} = Q. \end{aligned}\right\} \tag{4.7}$$

The last equation is obtained by matching the flow in the interior to that in the Ekman layers (Prandtl 1952), where the *average* (with respect to z) flow has the same form as the corresponding irrotational flow that would occur in the absence of end walls, but is $D_0/2(\nu/\Omega)^{\frac{1}{2}}$ times as rapid, where D_0 is the uniform distance between the end walls (see figure 4).

Axial motion is confined to boundary layers of thickness Δ_E and Δ_K respectively on the source and sink. Inspection of (4.6) (when applied to the case now under discussion, namely $\nabla_1 D = 0$) suggests that, when non-linear terms such as $\bar{u}\,\partial\bar{\zeta}/\partial y$ can be ignored (and the flow is steady), both Δ_E and Δ_K are of order $\nu^{\frac{1}{4}}D_0^{\frac{1}{2}}/\Omega^{\frac{1}{4}}$ the Stewartson (1957) thickness; but when non-linear terms cannot be neglected, Δ_E and Δ_K are determined by two length scales, $\tilde{U}D_0/(\nu\Omega)^{\frac{1}{2}}$ (corresponding to a balance of the non-linear terms with the right-hand side of (4.6)) and $\nu/\tilde{U}$ (corresponding to a balance of the non-linear term with $\nu\nabla_1^2\bar{\zeta}$) where $\tilde{U}$ is a typical relative flow velocity, of order $|\nabla_1 A_z|$ in this case. The final theoretical preliminary to the experiments described below in §§6–8 will be to investigate as carefully as possible the dependence of Δ_E and Δ_K, the thicknesses of the side-wall

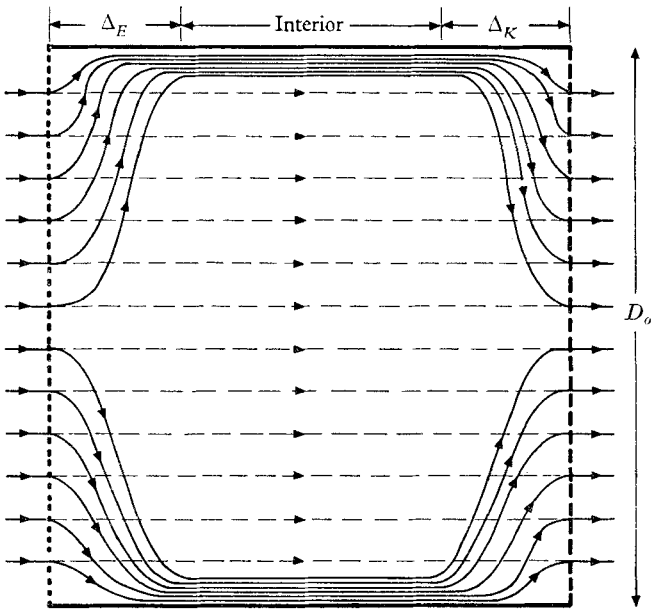

(*a*)

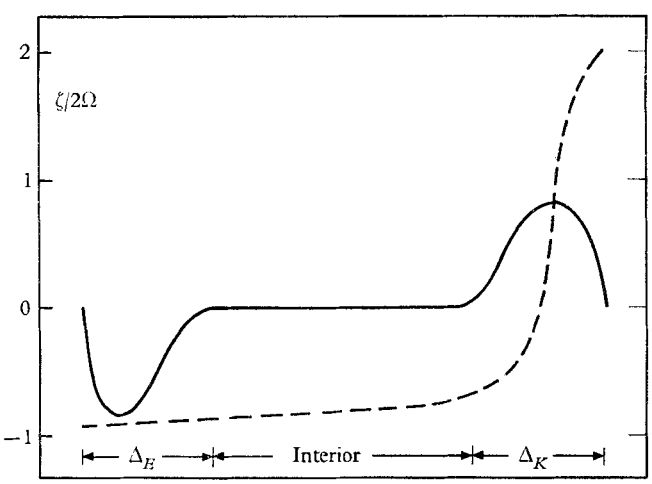

(*b*)

FIGURE 4. The effect of end walls in $z = 0$ and $z = D_o$ on flows due to distributions of sources and sinks for which $j \neq 0$, see figure 3. (*a*) shows the projection of streamlines on an arbitrary surface that everywhere lies parallel to $\boldsymbol{\Omega}$ and intersects the surfaces of the source and of the sink in the heavy dotted and dashed lines respectively (cf. figure 1). (*b*) shows the corresponding variation of relative vorticity, ζ, across the same surface in regions remote from the end-wall boundary layers. The lightly dashed line corresponds to the case when end-walls are absent, the full lines when end walls are present. When $|Q/2\pi D_o \nu|$, a Reynolds number R, is much greater than unity (see (A 3)), ζ in the absence of end walls is very close to -2Ω everywhere except within a boundary layer of thickness proportional to R^{-1} on the sink, where ζ attains positive values of order $R\Omega$ (cf. (A 4) and figure A 1). Suction due to the Ekman boundary layers, 95 % thickness $3(\nu/\Omega)^{\frac{1}{2}}$, that occur on the end walls reduces $\nabla_1\phi$ and ζ to zero in the interior region (cf. (2.1) and (4.7)), and gives rise to axial motion in boundary layers of thickness Δ_E and Δ_K on the surfaces of the source and sink (see (5.11)).

boundary layers, on the external parameters, over that range of parameters for which the end-wall boundary layers have the Ekman thickness, $\delta = 3(\nu/\Omega)^{\frac{1}{2}}$ (see (2.9)).

5. Side-wall boundary layers

A complete theory of the detailed structure of the side-wall boundary layers lies beyond the scope of this paper, although the following analysis might ultimately prove useful as a starting-point. We restrict attention here to an axisymmetric annular system (see figure 3*a*), i.e.

$$\left.\begin{aligned} f(P) &= Q/2\pi a D_o \quad \text{on} \quad g_1(x,y) = (x^2+y^2-a^2) = 0, \\ f(P) &= Q/2\pi b D_o \quad \text{on} \quad g_2(x,y) = (x^2+y^2-b^2) = 0, \\ m &= 2, j' = 2, j = 1 \end{aligned}\right\} \tag{5.1}$$

(see (3.3)); the corresponding flow in the absence of end effects is that described by the exact solution presented in the appendix. Then, the azimuthal components of the equations of steady motion and the equation of continuity reduce to

$$U\left[2\Omega + \frac{1}{r}\frac{\partial}{\partial r}(Vr)\right] + W\frac{\partial V}{\partial z} = \nu\left\{\frac{\partial}{\partial r}\left(\frac{1}{r}\frac{\partial (Vr)}{\partial r}\right) + \frac{\partial^2 V}{\partial z^2}\right\} \tag{5.2}$$

and

$$\frac{1}{r}\frac{\partial}{\partial r}(Ur) + \frac{\partial W}{\partial z} = 0, \tag{5.3}$$

(U, V, W) being, respectively, the radial, azimuthal and axial components of $\mathbf{u}$ at a general point with cylindrical polar co-ordinates (r, θ, z) (see (2.3) and (2.2)). The problem simplifies further when

$$\Delta_E \gg 3(\nu/\Omega)^{\frac{1}{2}} \quad \text{and} \quad \Delta_K \gg 3(\nu/\Omega)^{\frac{1}{2}}, \tag{5.4}$$

because the Ekman layers on the end walls (see (2.9)) are then much thinner than the boundary layers on the side walls and may therefore be assumed to extend well into the corner regions (see figure 4).

Under the foregoing simplifications, and the additional one that the side-wall boundary-layer thickness, Δ_E or Δ_K, is much less than the corresponding radius of curvature of the side wall, a or b as the case may be, we can write

$$Ur = \frac{Q}{2\pi D_o}\left[\exp\left(\frac{3(a-r)}{\Delta_E}\right) + \exp\left(\frac{3(r-b)}{\Delta_K}\right) + \frac{3D_o}{\delta}\exp\left(\frac{3(z-z_u)}{\delta}\right)\sin\left(\frac{3(z_u-z)}{\delta}\right) - \frac{3D_o}{\delta}\exp\left(\frac{3(z_l-z)}{\delta}\right)\sin\left(\frac{3(z-z_l)}{\delta}\right)\right] \tag{5.5a}$$

and

$$Vr = \frac{3Q}{2\pi\delta}\left[\exp\left(\frac{3(a-r)}{\Delta_E}\right) + \exp\left(\frac{3(r-b)}{\Delta_K}\right) - 1\right] \times \left[1 - \exp\left(\frac{3(z-z_u)}{\delta}\right)\cos\left(\frac{3(z_u-z)}{\delta}\right) - \exp\left(\frac{3(z_l-z)}{\delta}\right)\cos\left(\frac{3(z-z_l)}{\delta}\right)\right] \tag{5.5b}$$

as approximate expressions for Ur and Vr (cf. (3.3) and (4.7)), supposing that the inner cylinder is the source and the outer cylinder the sink. (For the corresponding expressions when the source and sink are reversed, interchange Δ_E and Δ_K in (5.5) and replace Q by $-Q$.)

All the exponential terms in (5.5) vanish in the interior regions, where

$$U = 0, \quad Vr = -Q\Omega^{\frac{1}{2}}/2\pi\nu^{\frac{1}{2}}. \tag{5.6}$$

The terms involving $(z-z_u)$ and (z_l-z) represent the exponentially damped axial variations in the Ekman boundary layers on the end walls. The maximum error due to neglecting non-linear terms in the equations of motion for the Ekman layer (see (5.2)) is of the order of a Rossby number

$$\epsilon \equiv Q/2\pi\nu^{\frac{1}{2}}\Omega^{\frac{1}{2}}a^2 \tag{5.7}$$

based on the azimuthal flow in the interior and on a. The terms involving $(r-b)$ and $(a-r)$ represent the radial variation in the side-wall boundary layers, assumed for simplicity to be exponential, with no oscillations. At $r = (a+\Delta_E)$ and $r = (b-\Delta_K)$ (and z well outside the Ekman layers), $|Ur|$ is only 0·05 ($\doteqdot \exp(-3)$) of its value at the neighbouring boundary, $r = a$ or $r = b$, and $|Vr|$ has risen to 0·95 ($\doteqdot 1-\exp(-3)$) of its interior value (see figure 4) given by (5.6). As we shall see below, even when $\epsilon \ll 1$ non-linear terms cannot be ignored in the equations governing the flow in the side-wall boundary layers unless the dimensionless parameter

$$X_a \equiv Q/6\pi\sqrt{2}aD_o^{\frac{1}{2}}\nu^{\frac{3}{4}}\Omega^{\frac{1}{4}} \tag{5.8}$$

(with a similar expression for X_b) is much less than unity (cf. (2.11)).

By (5.3), the continuity equation, and (5.5a),

$$\begin{aligned} Wr = \frac{3Q}{2\pi}G(r)\left[\frac{z}{D_o}-\frac{1}{2}\right]\left\{\frac{1}{\Delta_E}\exp\left(\frac{3(a-r)}{\Delta_E}\right)-\frac{1}{\Delta_K}\exp\left(\frac{3(r-b)}{\Delta_K}\right)\right\} \\ \times\left\{1-\exp\left(\frac{3(z-z_u)}{\delta}\right)\cos\left(\frac{3(z_a-z)}{\delta}\right)\right\}\left\{1-\exp\left(\frac{(3(z_l-z)}{\delta}\right)\cos\left(\frac{3(z-z_l)}{\delta}\right)\right\}, \end{aligned} \tag{5.9}$$

where $G(r)$, which vanishes on $r = a$ and $r = b$, has been introduced in order to satisfy the no-slip boundary condition (3.2a). As the term involving W in (5.2) can safely be neglected when V is of the form given by (5.5b), we can evaluate Δ_E and Δ_K under the assumptions made above without having to discuss $G(r)$. (Suffice it to remark here that, when $X \ll 1$, the boundary-layer substructure represented by $G(r)$ is characterized by the length scale $D_o^{\frac{1}{3}}\nu^{\frac{1}{3}}/\Omega^{\frac{1}{3}}$, which is less than Δ_E and Δ_K, then of order $D_o^{\frac{1}{2}}\nu^{\frac{1}{4}}/\Omega^{\frac{1}{4}}$ (see (5.14b), also Lewellen 1965; Rott & Lewellen 1966; Proudman 1956; Stewartson 1957). The determination of this substructure when $X \not\ll 1$ is a significant unsolved problem.)

Now substitute (5.5) in (5.2) and find for the dimensionless measure of Δ_E and Δ_K, namely

$$(Z_E, Z_K) \equiv \left(\frac{\sqrt{2}\,\Omega^{\frac{1}{4}}}{3\nu^{\frac{1}{4}}D_o^{\frac{1}{2}}}\right)(\Delta_E, \Delta_K), \tag{5.10}$$

the following equations:

$$\left.\begin{aligned} Z_E^2 - 3X_aZ_E\exp\left[3(a-r)/\Delta_E\right]-1 = 0, \\ Z_K^2 + 3X_bZ_K\exp\left[3(r-b)/\Delta_K\right]-1 = 0. \end{aligned}\right\} \tag{5.11}$$

The dimensionless parameter X_a or X_b (see (5.8)) measures the ratio of the magnitude of the non-linear term in (5.2) to that of the viscous term. It is a Rossby

number based on the speed of azimuthal flow in the interior (see (5.6)) and on the Stewartson (1957) thickness $3\nu^{\frac{1}{4}}D_o^{\frac{1}{2}}/\sqrt{2}\,\Omega^{\frac{1}{4}}$; it is also a Reynolds number based on the speed equal to one-ninth of U at the side walls and on the Stewartson thickness. When non-linear effects are negligible we can set $X_a = X_b = 0$ in (5.11), which then have (acceptable) solutions $Z_E = Z_K = 1$. Hence, and in agreement with an analysis of the linear case by Lewellen (1965), both side-wall boundary layers then have the Stewartson thickness.

The non-linear case is of greater interest in connexion with the experiments. Approximate the exponential term in each of (5.11) by 0·333, its average value over the range of r for which the term exceeds 0·05, and thus find

$$\left.\begin{aligned} Z_E^2 - X_a Z_E - 1 &= 0, \\ Z_K^2 + X_b Z_K - 1 &= 0. \end{aligned}\right\} \tag{5.12}$$

The acceptable solutions of these equations, namely

$$Z_E = (1 + \tfrac{1}{4}X_a^2)^{\frac{1}{2}} + \tfrac{1}{2}X_a, \tag{5.13a}$$

$$Z_K = (1 + \tfrac{1}{4}X_b^2)^{\frac{1}{2}} - \tfrac{1}{2}X_b, \tag{5.13b}$$

are such that $Z_E = Z_K = 1$ when $X_a = X_b = 0$; and $Z_E = X_a$ and $Z_K = X_b^{-1}$ when $X_a \gg 1$ and $X_b \gg 1$.

Equations (5.13) are illustrated in figure 5, which shows that Δ_E increases and Δ_K decreases with increasing X, the asymptotic expressions for these quantities being

$$\left.\begin{aligned} \Delta_E &= \frac{Q}{4\pi a \nu^{\frac{1}{2}}\Omega^{\frac{1}{2}}} \quad \text{when} \quad X_a \gg 1, \\ \Delta_K &= \frac{18\pi b D_0 \nu}{Q} \quad \text{when} \quad X_b \gg 1) \end{aligned}\right\} \tag{5.14a}$$

(cf. the closing remarks of §4), which should be compared with

$$\left.\begin{aligned} \Delta_E &= 3\nu^{\frac{1}{4}}D_o^{\frac{1}{2}}/\sqrt{2}\,\Omega^{\frac{1}{4}} \quad \text{when} \quad X_a \ll 1, \\ \Delta_K &= 3\nu^{\frac{1}{4}}D_o^{\frac{1}{2}}/\sqrt{2}\,\Omega^{\frac{1}{4}} \quad \text{when} \quad X_b \ll 1. \end{aligned}\right\} \tag{5.14b}$$

The interpretation of (5.14a) is straightforward. In the boundary layer on the source, thickness Δ_E, viscous forces are negligible when $X_a \gg 1$, implying conservation of angular momentum, as expressed by the balance

$$2\Omega + r^{-1}\partial(Vr)/\partial r = 0$$

(see (5.3)). Non-viscous forces are capable of bringing about the change in the solenoidal component of velocity (namely V in this axisymmetric case) that a particle must experience in passing from the surface of the source, where V is zero, to the other side of the side-wall boundary layer, where V is non-zero (and negative in the case under discussion, see figure 4 and (5.6)). ν enters the expression for Δ_E (as $\nu^{-\frac{1}{2}}$) only through the requirement that in the corner regions (see figure 4) $\mathbf{u}$ in the boundary layer on the side walls must match $\mathbf{u}$ in the Ekman boundary layers on the end walls.

As a fluid particle traverses the boundary layer on the *sink*, thickness Δ_K, it must experience an *increase* in azimuthal velocity if V is to vanish at the wall.

Because non-viscous forces can only produce a *decrease* in V, Δ_K must be sufficiently small for viscous forces to attain sufficient strength to bring about the required increase in V. $Ur^{-1}\partial(Vr)/\partial r = \nu\partial(r^{-1}\partial(Vr)/\partial r)/\partial r$ is then the essential balance of forces in (5.2), the corresponding value of Δ_K being proportional to ν/Q and independent of Ω (see (5.14a)).

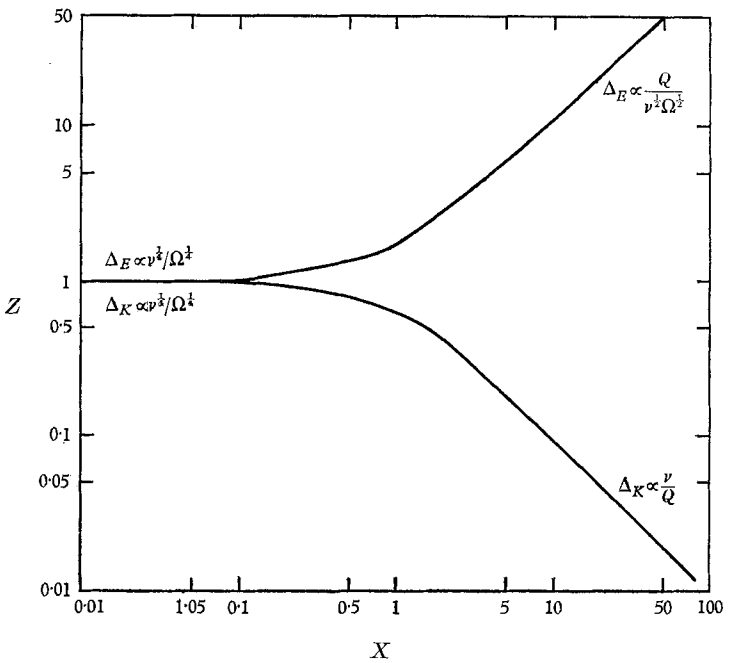

FIGURE 5. The dependence of Δ_E (upper curve) and Δ_K (lower curve) on Q (cf. figure 4). Z is a dimensionless measure of Δ_E or Δ_K (see (5.10)). $X \equiv Q/3\sqrt{2}L_s D_0^{\frac{1}{2}}\nu^{\frac{3}{2}}\Omega^{\frac{1}{2}}$ is a dimensionless measure of Q and thus measures non-linear effects (see (5.8)). The equations of the upper and lower curves are $Z = (1+\frac{1}{4}X^2)^{\frac{1}{2}} \pm \frac{1}{2}X$ respectively (see (5.13)); their ranges of validity are given by (5.15)–(5.17).

When the flow in the system is directed radially *inward* rather than outward (cf. figure 4), (5.5), (5.6) and (5.9) still hold for U, V and W if we write $-Q$ for Q, and (5.10) to (5.13) hold for Z_E and Z_K if we interchange X_a and X_b. Equations (5.10)–(5.13) bring out the essential non-linearity of the system for, except when $X \ll 1$, reversing the direction of flow through the system changes the character of each side-wall boundary layer.

It will be important to extend the foregoing analysis to non-axisymmetric systems. The basic lengths will still be the same as those given by the right-hand sides of (5.14), but the dependence of Δ_E and Δ_K on these lengths will, in general, differ from (5.14), except when $X \ll 1$.

Range of validity of equations (5.13)

The use in (5.5) of exponential functions for describing the r dependence of (U, V, W) is unlikely to be valid except when

$$\Delta_E \ll a \quad \text{and} \quad \Delta_K \ll b, \tag{5.15}$$

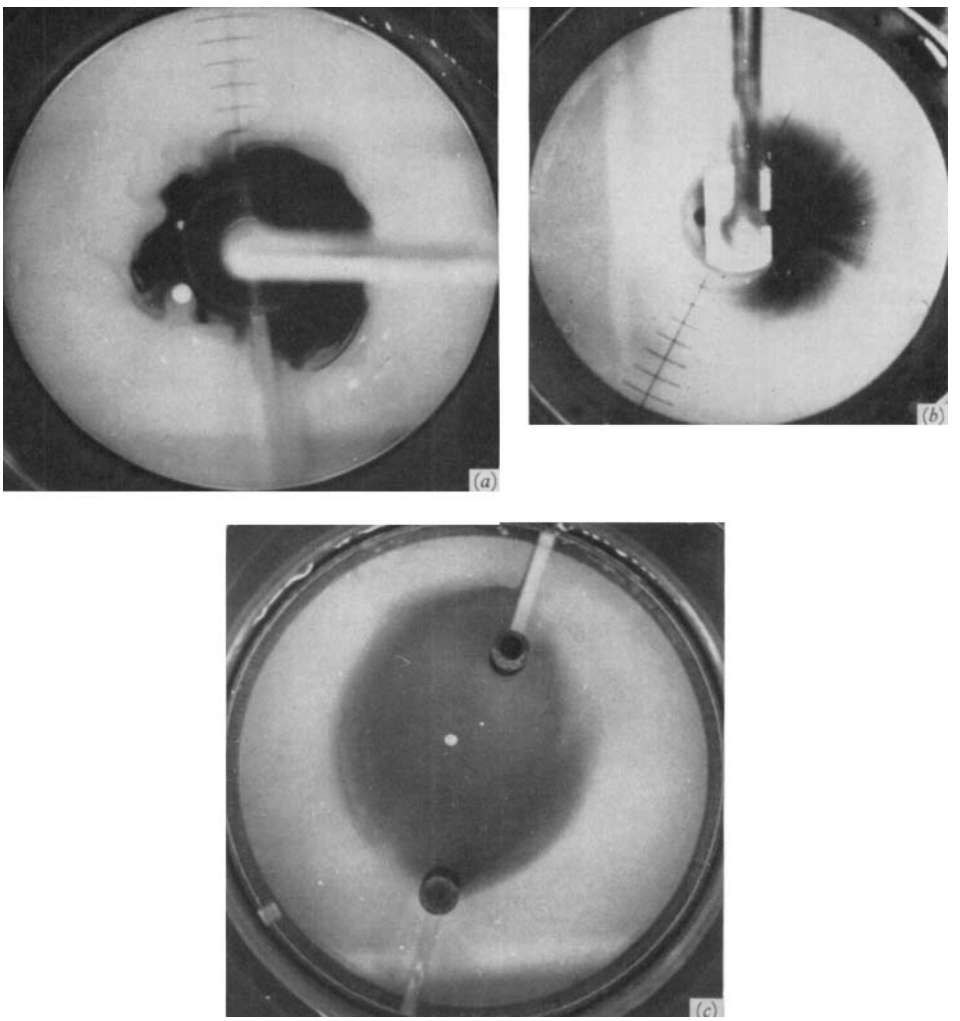

FIGURE 6. Three examples of flows due to source–sink distributions for which $j = 0$, the key to the arrangements of sources, sinks and impermeable surfaces being given, in order, by figures 2*a*, *b* and *c*. Each photograph was taken several minutes after dyed fluid first entered the system via the source. In each case, notwithstanding the rapid rotation of the whole apparatus, at speeds of over 10^3 times the typical speeds at which fluid passed through the working region, **u** was virtually unaffected by rotation. (The dye pattern in (*a*) is the result of entirely radial motion on an initial dye distribution which possessed azimuthal variations.) Ekman layers were present, presumably, on the end walls, but they were too thin to have produced visible effects in these photographs. (Depth D uniform; for full experimental details see table 1 and §§ 6 and 7.

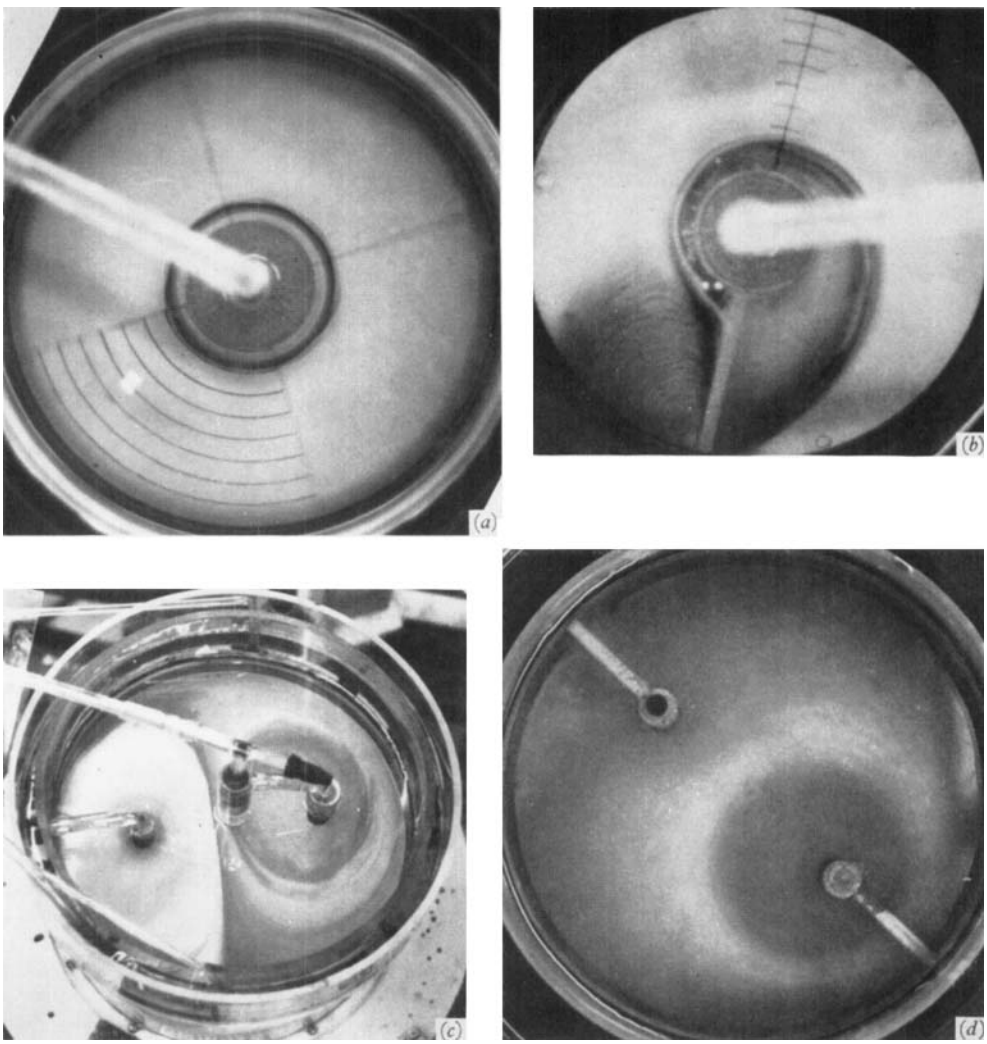

FIGURE 7. Four examples of flows due to source–sink distributions for which $j \neq 0$, the key to the arrangement of sources and sinks and impermeable surfaces being given, in order, by figures 3*a–d*. Each photograph was taken several minutes after dyed fluid first entered the system via the source. The gyres present in each case indicate directly that, in contrast to the case $j = 0$, when $j \neq 0$ $\mathbf{u}$ in the main body of the fluid depends on Ω. Moreover, effects due to viscous Ekman boundary layers on the end walls profoundly influence the flow in the main body of the fluid in the manner illustrated by figure 4 (see figure 8). (Depth D uniform; for full experimental details see table 1 and §§6 and 7.)

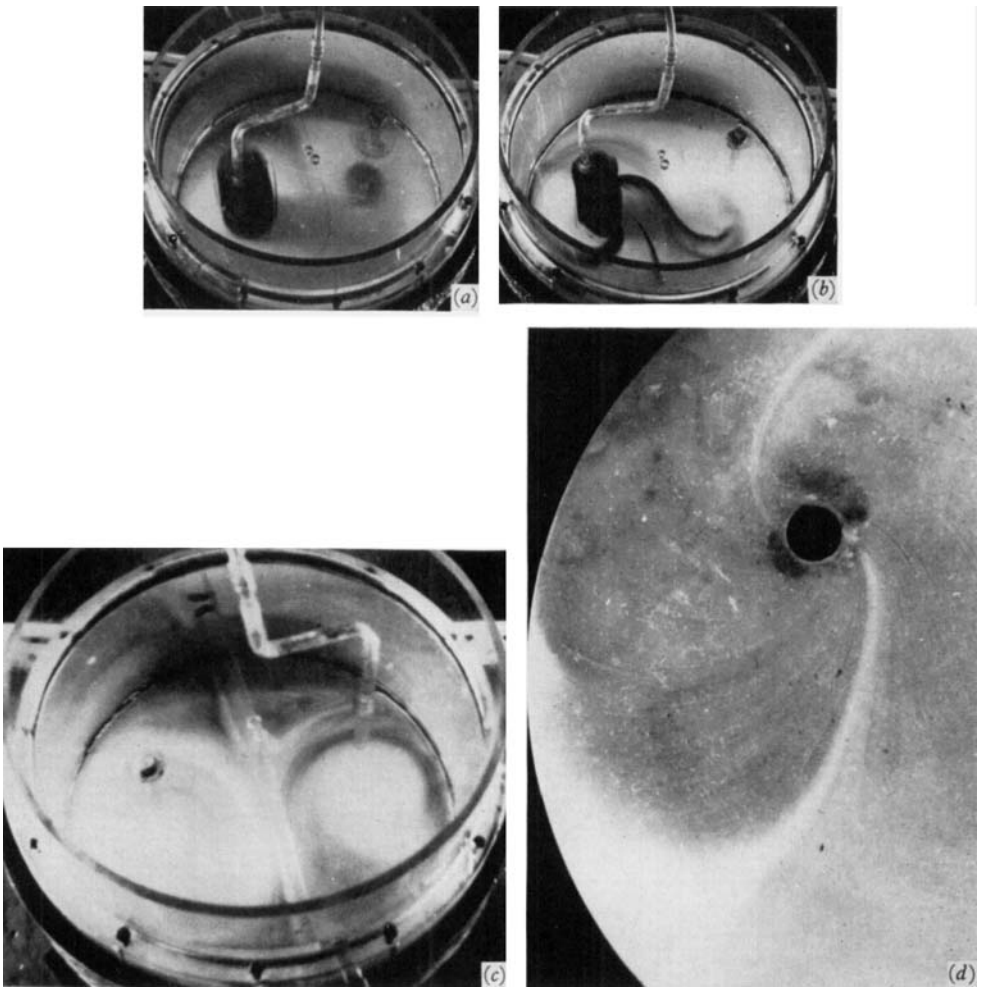

FIGURE 8. Further details of the flow illustrated in figure 7*c*. In (*a*) and (*b*) fluid was introduced and withdrawn from the working region via two short tubes, the source being on the left in each case. Both pictures indicate that axial motion occurs only in the vicinity of the source and sink. In (*b*) dye produced by a crystal of nigrosine placed on the floor on the tank gave rise to the curved streaks in the direction of the mean flow in the bottom Ekman layer (cf. figure 4). The third picture, (*c*), which should be compared with figure 7*c* (see also figures 8*a* and 8*b*), shows that the flow is unaffected by the introduction of a rigid impermeable barrier at the boundary of contact between the two gyres in the 'interior' region (provided that the combined width of the gaps that were left between barrier and the end walls in $z = 0$ and $z = D_o$, though much less than D_o, was not too small, i.e. not less than the Ekman-layer thickness, $3(\nu/\Omega)^{\frac{1}{2}}$). The fourth picture, (*d*), indicates the pattern of flow in the Ekman layer on the end wall, as revealed by the crystal violet etching technique described in § 6. (See table 1 for full experimental details.)

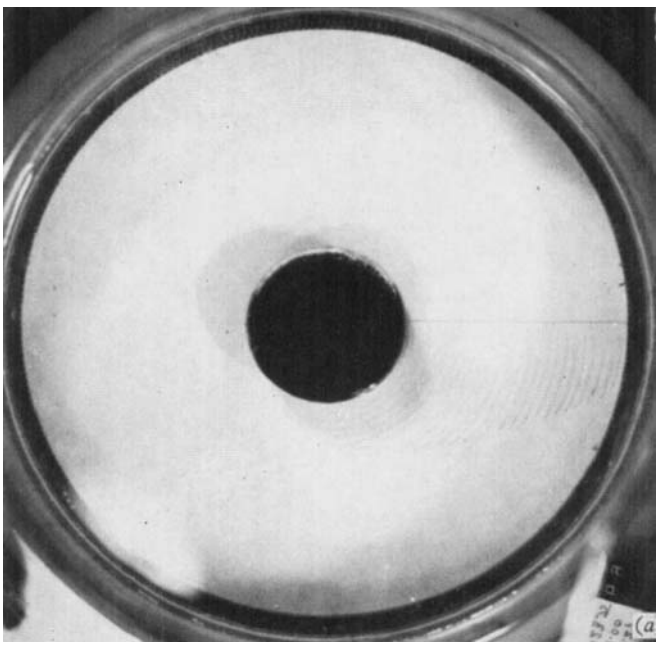

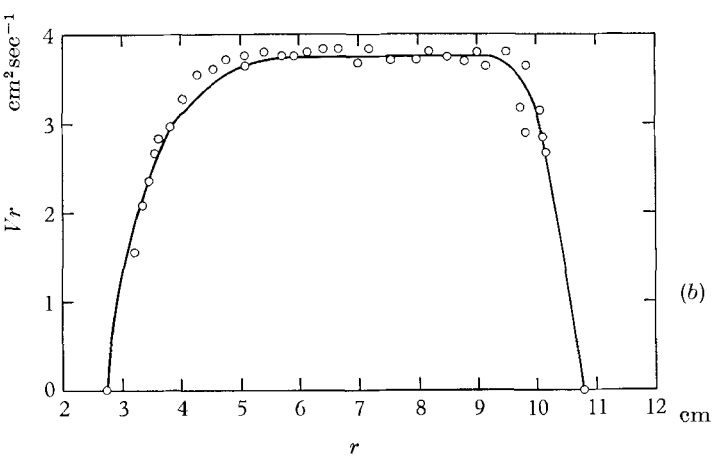

FIGURE 9. Observations of the azimuthal component of the flow due to an annular source–sink arrangement illustrated by figure 3*a* (cf. figures 7*a* and 10*a*). (*a*) is a photograph of dye streaks released from equally spaced points on a thin (0·004 in. diameter) copper wire, using the iodine-starch technique described in § 6. The points in (*b*) are based on determinations of Vr from several photographs such as (*a*), and the line is a theoretical curve based on (5.5*b*), with Δ_E and Δ_K given by (5.10) and (5.13). (Depth D uniform; see table 1 for full experimental details.)

and we can expect *quantitative* errors from this procedure and from the averaging procedure leading from (5.11) to (5.12). Equations (5.13) must break down *qualitatively* when non-linear effects in the end-wall boundary layers, in magnitude of order ϵ times the linear effects (see (5.7)), cannot be neglected; this consideration restricts the range of validity of (5.13) to values of X_a satisfying

$$X_a \ll \frac{a\Omega^{\frac{1}{2}}}{3\sqrt{2}\,\nu^{\frac{1}{2}} D_o^{\frac{1}{2}}}. \tag{5.16}$$

The assumption that the side-wall boundary layers are thicker than the Ekman layers on the end walls (see (5.4)) requires that

$$X_a \ll \frac{D_o^{\frac{1}{2}}\Omega^{\frac{1}{4}}}{\sqrt{2}\,\nu^{\frac{1}{4}}}. \tag{5.17}$$

The last two restrictions are by no means prohibitive; while the typical values of the right-hand sides of (5.16) and (5.17) may greatly exceed unity, the largest value of X attained in the experiments was 2·2.

This completes the theoretical part of the paper, and we are now in a position to present the experiments.

6. Apparatus and techniques

The main apparatus consisted of a cylindrical Perspex (Plexiglas) tank of inside diameter 30 cm, constructed in such a way that the permeable and impermeable bounding surfaces of the 'working region' of the fluid (see figures 2 and 3) in the tank could be changed without too much difficulty.

The tank was mounted on a horizontal turntable with its vertical axis coincident with the rotation axis of the turntable. The turntable was driven with angular speed Ω, usually between 1 and 4 rad/sec (see table 1), by means of a continuously variable speed motor and gear-box arrangement. Ω was determined to better than 0·5 % by means of an electronic timing device actuated by the pulse generated once per revolution of the turntable when the beam from the lamp mounted on the turntable fell onto a photocell fixed in the laboratory. Variations in Ω never amounted to more than 1 % over periods of several hours.

The 'working region' of the rotating tank formed part of a circuit through which fluid passed at a constant rate, Q, typical values of which were between 0·45 and 2·27 cm^3/sec. After some preliminary trials, a system that proved successful consisted of a 'constant head' tank, capacity 40 l, mounted about 2 m above the working region, from which fluid passed under gravity to the working region via a shut-off valve, a 10-turn needle valve, a 'manostat-Predictability' flowmeter, a motor-actuated ball-float mechanism, and a second shut-off valve, all connected in series. With this arrangement fluctuations in Q never exceeded 2 % and were usually much less. The error in the determinations of Q ranged from 0·5 % at the highest values used to 2 % at the lowest values (see table 1).

Water was the fluid used in all the experiments reported below. Although the viscosity of water depends strongly on temperature, by controlling the ambient temperature as carefully as possible, variations in ν during any single experiment were kept under 1 %.

Excepting the case illustrated by figure 13*c* (see also table 1) (for which Ω was much less, by at least an order of magnitude, than in the other experiments, the corresponding value of the Ekman number,

$$\gamma \equiv \nu/\Omega\bar{D}^2, \tag{6.1}$$

$\bar{D}$ being the average value of $D(x, y)$, and that of the Rossby number ϵ (see (5.7)) being, respectively, 10^{-2} and 1 approximately), typical values of γ and ϵ were

Figure	(Key[1])	Source[2]	Sink[2]	Mean depth (cm)	Ω (rad/sec)	Q (cm^3/sec)	Dye[6]
6*a*	(2*a*)	2.71 C	11·36 F	2·90[3]	2·00	1·33	n
b[7]	(2*b*)	2·71 C	2·71 C	2·90[3]	2·00	0·45	n
c	(2*c*)	0·8 B	0·8 B	4·85[3]	1·33	1·33	n
7*a*	(3*a*)	2·71 D	10·83 C	4·85[3]	2·00	2·27	n
b	(3*b*)	2·71 D	11·36 C	2·90[3]	2·00	1·33	n
c	(3*c*)	0·8 B	0·8 B	16·9[3]	2·0	1·0	n
d	(3*d*)	0·8 B	0·8 B	4·85[3]	4·8	2·27	p
8*a*	(3*c*)	0·32 A	0·32 A	16·9[3]	2·96	1·05	n
b	(3*c*)	0·32 A	0·32 A	16·9[3]	2·98	2·11	n
c	(3*c*)	0·32 A	0·32 A	16·9[3]	4·23	1·0	n
d[7]	(3*c*)	0·8 B	0·8 B	16·9[3]	2·0	1·0	v
9*a*	(3*a*)	2·71 E	10·83 C	4·85[3]	1·00	2·27	s
10*a*	(3*a*)	2·71 D	10·83 C	4·85[3]	4·00	2·27	n
b	(3*a*)	2·71 D	10·83 C	4·85[3]	4·00	1·33	n
c	(3*a*)	2·71 D	10·83 C	4·85[3]	4·00	0·45	n
d	(3*a*)	2·71 D	10·83 C	4·85[3]	2·00	2·27	n
e	(3*a*)	2·71 D	10·83 C	4·85[3]	1·00	1·33	n
f	(3*a*)	2·71 D	10·83 C	4·85[3]	1·00	0·45	n
12*a*	(3*a*)	2·71 E	10·83 C	4.13[4]	1·00	1·33	n
b	(2*a*)	2·71 E	10·83 C	4·13[4]	4·00	2·27	n
c	(2*a*)	2·71 E	10·83 C	4·13[5]	4·00	2·27	p
d	(3*c*)	0·32 A	0·32 A	16·9[5]	1·82	0·4	s
13*a*	(3*a*)	2.71 E	10·83 C	4·13[4]	1·00	1·33	n
b	(3*a*)	2·71 E	10·83 C	4·13[4]	1·00	1·33	n
c	(3*b*)	2·71 D	11·36 F	2·90[3]	0·067	2·27	n

[1] The 'key' number is that of the figure illustrating the source–sink arrangement used.

[2] The number gives the radius of curvature of the surface of the source or sink (as the case may be) in centimetres. The letter indicates the method of construction of the source or sink, thus: A, projecting tube; B, sintered brass; C, perforated Perspex cylinder; D, perforated Perspex cylinder filled with glass beads; E, perforated Perspex cylinder surrounded by gauze and filled with plastic foam; F, perforated aluminium cylinder.

[3] Depth D (see (2.13)), uniform; $dz_u/dr = dz_l/dr = 0$.

[4] Depth non-uniform; $dz_u/dr = 0$, $\tan^{-1}(dz_l/dr) = 10°$.

[5] Depth non-uniform; $dz_u/dr = 0$, $\tan^{-1}(dz_l/dr) = -10°$.

[6] Key to flow visualization technique used is as follows: n, nigrosine; p, phenolphthalein pH indicator; v, crystal violet etching; s, iodine-starch electrolyte technique (see § 6).

[7] Figures 6*b* and 8*d* were included in a recent review paper (Hide 1966).

TABLE 1

always a good deal less than unity. These values can be readily calculated from the data given above and in table 1, which summarizes the conditions of the experiments illustrated by the various photographs of flow patterns presented in figures 6–13.

During the course of the work, experience was gained in the design of permeable surfaces via which fluid could be introduced into and withdrawn from the working region. Owing to the high values of Ω and low values of Q used in the experiments, injection or withdrawal of fluid via a hole in one of the end walls or at the end of a narrow tube projecting into the working region was sufficient for qualitative investigations, and this method was employed during the early stages of the work (see figures 8*a–c*). Owing to the constraints of rotation, on entering the working region fluid would spread out much more rapidly in the axial direction than in the transverse directions, forming, effectively, a cylindrical source of somewhat larger transverse dimensions than the diameter of the hole. Similar effects, which are clearly seen in figure 8*a*, arose in the exit region. Although these effects are of interest in themselves (see Herbert 1965; Rott & Lewellen 1966; Barcilon 1967), we shall not consider them further here.

When it was necessary to know the exact dimensions of the 'working region' various types of rigid permeable materials were used, such as sintered brass tubing (used in motor-car petrol filters) (see figures 6*c*, 7*c*, *d*, 8*d*) and perforated Perspex or aluminium covered with thin wire mesh or cotton gauze. Axial variations in effective porosity were minimized by forcing the fluid to pass through glass beads (see figures 7*a*, *b*, 10*a–f*, 13*c*) or, better still, sponge or expanded plastic foam (see figures 12*a–c*, 13*a*, *b*) just before (after) entering (leaving) the working region via the surface of the source (sink). (Rigid, porous, machinable plastics are being used in an extension of the present work.)

Several flow visualization techniques were used during the course of the experiments. One of these involved colouring the fluid with a neutrally buoyant dye (nigrosine in water and alcohol (see figures 6*a–c*, 7*a–c*, 8*a–c*, 10*a–f*, 12*a*, *b*, 13*a–c*) or fluorescein) as it approached the working region. Another technique involved the production of dye at an electrode which either formed one of the bounding surfaces of the working region or was a taut, thin wire placed within the fluid (see figures 9*a* and 12*d*). The fluid was rendered electrically conducting by the addition of a small quantity of potassium iodide. By also adding a small quantity of starch, dye, in sufficient quantity to give a visual indication of the flow without disturbing it, could be produced by applying a d.c. voltage across the electrodes for about a second.

Yet another technique involved detecting, by means of the indicator phenolphthalein, changes in pH of the fluid in the working region resulting from the introduction of small quantities of an aqueous solution of calcium carbonate and ammonium hydroxide into the fluid circuit upstream of the working region (see figures 7*d* and 12*c*).

One of the pictures reproduced below (figure 8*d*) was obtained by means of a novel technique developed during the course of the present work. The surface of the end wall was painted with 'Krylon' spray acrylic paint. When the paint had dried, the surface was rendered matt by rubbing it with cotton soaked in alcohol,

which apparently removed the paint filler. In this condition, as was found more or less accidentally by my assistant, Mr Bernard Gray, the matt surface was readily stained by crystal violet dye. On introducing crystal violet dye into the fluid, the pattern of dye in the fluid near the end wall, which was determined by the flow pattern there, gave rise to a similar pattern on the painted surface.

The camera used to obtain the photographs presented in figures 6–13 pointed either exactly or approximately in the direction of the negative z-axis, the sense, as seen in the diagrams, of the basic rotation being counter-clockwise in all cases. The upper surface of the working region was always plane and horizontal. The lower surface was plane and horizontal in all the experiments excepting those illustrated by figures 12*a–d*, 13*a* and *b*, when the bottom sloped at 10° (figures 12*a*, *b*, 13*a*, *b*) or $-10°$ (figures 12*c*, *d*) to the horizontal.

7. Experiments with containers of uniform depth ($\nabla_1 D = 0$)

When the depth of the fluid container is uniform (i.e., $\nabla_1 D\,(x, y) = 0$), and equal to D_0, the non-viscous contribution, proportional to $\bar{\mathbf{u}}.\nabla_1 D(x, y)$, to the expression for the vorticity changes in the interior region due to the presence of end walls vanishes for any $\mathbf{u}$ (see right-hand side of (4.6)). When $\nu \neq 0$, the remaining contribution, proportional to $(\nu/\Omega)^{\frac{1}{2}}\bar{\zeta}$, vanishes only when $\bar{\zeta} = 0$. Thus, as shown in §4, we must distinguish between two general cases: case (i) for which the relative vorticity, $\nabla_1^2 A_z$, of the corresponding strictly two-dimensional flow is zero, and case (ii) for which $\nabla_1^2 A_z \neq 0$. According to §3 (see especially (3.17) and figures 2 and 3), cases (i) and (ii) correspond, respectively, to $j = 0$ and $j \neq 0$, where j is the number of irreducible sets of closed curves across which the net flow of fluid is non-zero. We shall discuss these two cases separately.

Case (i): $j = 0$

Three examples are illustrated in figure 6, plate 1, the corresponding key to the source–sink arrangements being given in figure 2. Each photograph was taken several minutes after dyed fluid first entered the system via the source. In each case, notwithstanding the rapid rotation of the whole apparatus at speeds of over 10^3 times the typical speed at which the fluid entered and left the working region, $\mathbf{u}$ in the main body of the fluid was irrotational and apparently unaffected by rotation, as theory predicts (see(3.14)–(3.19) and §4). (The dye pattern in, figure 6*a* is the result of an entirely radial motion on an initial dye distribution which possessed azimuthal variations.) Ekman layers were present, presumably, on the end walls, but because they were very thin in comparison with the total depth of the fluid they produced no visible effects in these photographs.

Although the cylindrical sources and sinks used in many of the experiments were designed so as to avoid variations in $f(P)$ (see (3.3)) over their surfaces (see §6 and figures 9*a*, 12*a–c*, 13*a*, *b*), such variations were only *completely* negligible when special precautions were taken (see table 1). Fortunately the effects of such variations penetrated only a short distance into the working region. Beyond this distance (which, according to work by Lewellen (1965) and Barcilon (1967), and in keeping with general ideas, should be of order $D_0^{\frac{1}{3}}\nu^{\frac{1}{3}}/\Omega^{\frac{1}{3}}$ cm when non-

linear effects are negligible), **u** was independent of z (except, of course, in the Ekman layers on the end walls). The theory of this penetration process when non-linear effects cannot be neglected does not seem to have been investigated.

Although no pressure measurements were made, evidence that an appreciable azimuthal pressure gradient was associated with the radial flow depicted by figure 6*a* is presented in figure 7*b*. The drop in p that forces fluid in the negative θ direction (i.e. 'westward,' from right to left in the lower part of figure 7*b*) through the gap in the radial barrier should, according to (A 7), fall short of $\Omega q/\pi$ by an amount that increases with increasing gap-width, and vanishes altogether when the radial barrier is removed (see (A 1), (5.5) and figure 7*a*).

Case (ii): $j \neq 0$

Four examples are illustrated in figure 7, plate 2 (see also figure 8, plate 3), the corresponding key to the source–sink arrangement being given in figure 3. Theory predicts that, in contrast to the other case, $j = 0$, when $j \neq 0$ the actual flows in the presence of plane, parallel end walls should differ considerably from their two-dimensional counterparts (see (3.18) and (4.7)), and the experiments confirm this prediction.

That the transport of fluid from source to sink takes place via the Ekman layers and not via the interior of the fluid, where $\nabla_1 \phi = 0$ (see (4.7)), was amply demonstrated in the experiment illustrated by figure 8*c* (cf. figures 7*c*, 8*a* and *b*). In that experiment it was shown that the flow is unaffected by the introduction of a rigid impermeable barrier at the boundary of contact between the two gyres, provided that the combined widths of the gaps between the barrier and the end walls near $z = 0$ and $z = D_o$, though much less than D_o, are not too small (i.e. not less than the Ekman layer thickness, $3(\nu/\Omega)^{\frac{1}{2}}$). Further verification of (4.7) is contained in figure 9, plate 4, where measurements of Vr are plotted against r.

Figure 10, plate 5, illustrates the width of the boundary layer on the source in an annular system (see figures 3*a*, 7*a*, 9) at several different values of Q and Ω. These observations were made as follows. For a short period of time (several minutes) the fluid was dyed before it entered the working region via the surface of the source. When viewed from along the axis of rotation the region occupied by the dye formed an annular ring which slowly grew in size until its outer radius had attained the value $(a+\Delta_E)$, beyond which point the ring of dye suffered virtually no further increase in size (cf. figure 4). z variations in the outer radius of the dyed region were slight (in keeping with (5.5)). It is noteworthy that, on stopping the supply of dye, the clearing that then occurred of the ring of dyed fluid on the source first became pronounced close to the surface of the source and then proceeded outwards.

One feature of the observed flow suggests that the theoretical flow pattern given in figure 4 is a slight over-simplification. In that diagram no re-circulation of fluid between the boundary layer on the source and the Ekman layer is indicated. Had re-circulation been absent in practice, the clearing of the dyed region would have eventually been complete. In fact, when the flow did not develop non-axisymmetric features a cylindrical sheet of dye remained long after the rest

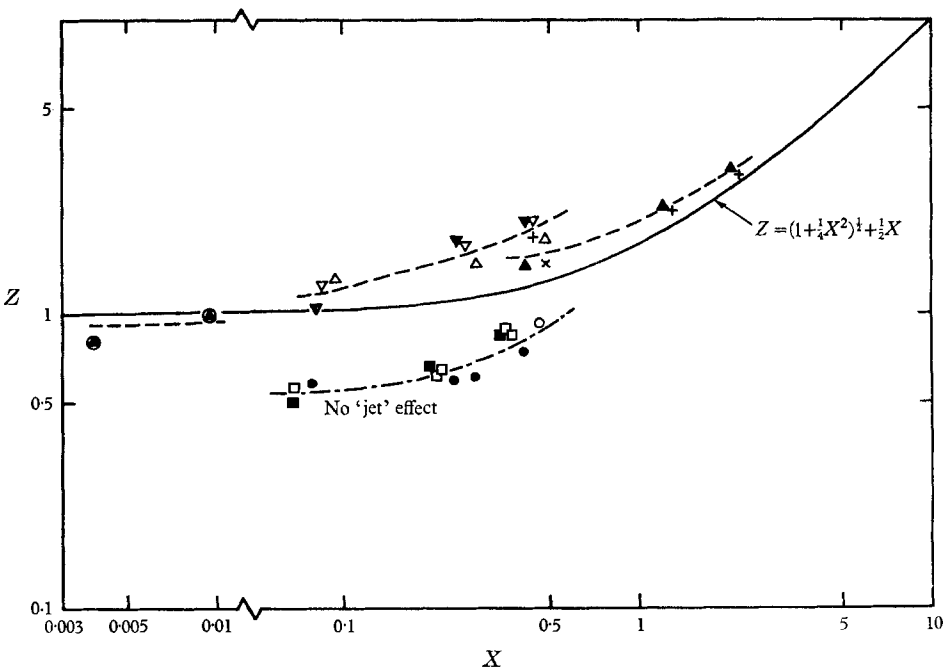

FIGURE 11. Experimental determinations of Z, the dimensionless thickness of the boundary layer on the source or sink, plotted against X, a dimensionless measure of Q (see (5.10) and (5.8), cf. figures 5, 9 and 10). The curve represents the dependence of Z on X predicted by the theoretical expression (5.13). The points at $X = 0{\cdot}0038$ and $X = 0{\cdot}0096$ are based on two determinations of the thickness of the boundary layer on the sink at $r = b$ obtained incidentally in another study (Hide, Ibbetson & Lighthill 1968). All the other points are for boundary layers on the source at $r = a$. The symbols have the following meaning:

Ω (rad/sec)	1·0	2·0	3·0	4·0	
D_0 (cm)					
4·06		×	+	▲	$a = 0{\cdot}485$ cm
4·85	○	●	□	■	$a = 2{\cdot}71$ cm
2·90		△	▽		$a = 2{\cdot}80$ cm
30·9		✪			$b = 14{\cdot}6$ cm

(Depth D uniform, see figure 10 and table 1 for full experimental details.)

DESCRIPTION OF PLATE 5

FIGURE 10. Illustrating the variation of Δ_E with Ω and Q, and the wave-like instabilities that arise in certain circumstances. (*a*), (*b*), (*c*) and (*d*) show the end view of the cylindrical sheet of dye that remained long after the axial flow in the boundary layer on the source had cleared the remainder of the nigrosine dye introduced earlier at the surface of the source. No cylindrical dye sheet formed in the cases illustrated by (*e*) and (*f*), which are pictures of the non-axisymmetric pattern of flow that then occurred, taken before axial flow in the boundary layer had completely removed the dye from that region. Values of Q and Ω are as follows:

	(*a*)	(*b*)	(*c*)	(*d*)	(*e*)	(*f*)
Q (cm³/sec)	2·27	1·33	0·45	2·27	1·33	0·45
Ω (rad/sec)	4·00	4·00	4·00	2·00	1·00	1·00

(Depth D uniform; see table 1 for full experimental details.)

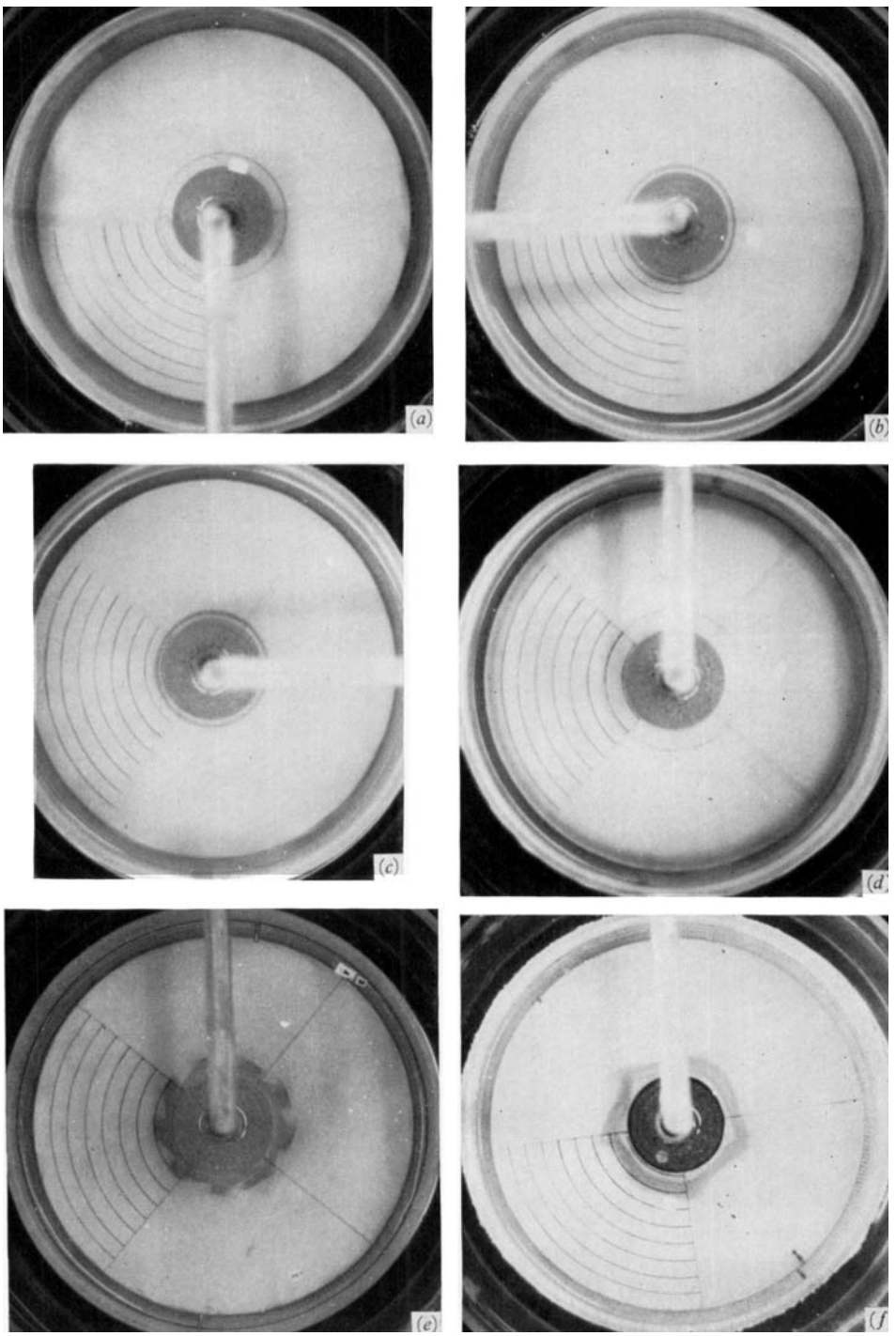

FIGURE 10. For legend see facing page.

of the dyed region had cleared (see figures 10*a–d*), suggesting that near the interface between the boundary layer on the source and the interior region axial motion *away* from the Ekman layers may have been taking place.

In the first part of the investigation of the thickness Δ_E of the boundary layer on the source, fluid entered the working region as small jets emerging from tiny holes in the perforated Perspex cylinder (see §6). The effect of these jets was to increase the effective radius of the cylindrical source. 'Jet effects' were eliminated in later work.

Δ_E was determined from measurements of the final value of the outer radius of the ring of dye. These determinations (uncorrected for the 'jet effects' that were present in all but one series of measurements) are given in figure 11, where Z, the thickness of the boundary layer divided by the Stewartson thickness, is plotted against X (see (5.10) and (5.8)).

These experimental results are consistent with several aspects of the theory presented in §§2–5 (although the experiments will have to be extended and the theory refined before a truly quantitative theoretical interpretation of the observations can be attempted). First, they support the conclusion that X is the dimensionless parameter in terms of which Q should be measured. Secondly, they confirm the prediction of the approximate theory (see (5.13)) that the thickness of a source boundary layer should increase with X; the experimental variation of Z with X is slightly more rapid, if anything, than the theoretical variation. Finally, they give values of Z which are of the same order of magnitude as the theoretical values, although it remains to be shown that the apparent discrepancy, of a factor of nearly 2, between theory and experiment is due to the neglect of curvature effects in the theory (see (5.15)).

This estimate of the discrepancy is based on the comparison of the theoretical curve representing equation (5.13) with the most reliable experimental determinations of Z, namely those for which 'jet effects' were absent (see figure 11). If 'jet effects' increase the effective size of the source by $(D_o\nu/\Omega)^{\frac{1}{2}}$ cm, these effects can be corrected for by reducing Z by the amount $(\nu/\Omega D_o^2)^{\frac{1}{12}}$ approximately, typical values of which are about 0·5. Simple considerations of geometrical convergence and divergence suggest that, owing to curvature effects, the thickness of a boundary layer on the inner cylinder should be $(1-\beta\Delta/a)$ times that given by (5.13), the corresponding factor for the outer cylinder being $(1+\beta\Delta/b)$, where β is a correction factor which is positive and less than unity.

Several instabilities were observed during the course of the experiments, but as the study of these instabilities was not the main objective of the present work, their detailed discussion will be given elsewhere on the completion of further experiments now in progress. A few general remarks are, however, in order.

In the experiments just described on the dependence of Δ_E on Q, Ω, etc., at certain values of Q and Ω the distribution of dye developed wave-like features as it emerged from the source (see figures 10*e* and *f*, plate 5). These non-axisymmetric features were manifestations, presumably, of non-axisymmetric instabilities of the basic axisymmetric flow in the boundary layer on the source (see figures 7*a* and 10*a–d*, plates 2 and 5). (Even in the case of figure 7*a*, the ring of dye is not quite axisymmetric.) The boundary layer on the sink

occasionally exhibited non-axisymmetric features even when the boundary layer on the source did not. There was evidence that these non-axisymmetric features may be inhibited or suppressed by the presence of a sloping bottom (cf. figures 10*e* and 12*a*, plates 5 and 6).

Evidence of *axisymmetric* instabilities was also found. In certain experiments (including some with containers of non-uniform depth, see figures 13*a* and 13*b*, plate 7) stationary concentric sheets of dye appeared in the interior region. The outer dye sheets usually appeared before the inner sheets (see figures 12*a*, 13*a*, *b*). These observations are reminiscent of those reported by Arons, Ingersoll & Green (1961) in their attempt to produce unstable Ekman layers, and it may be significant that typical values of the local Reynolds number in the Ekman layers, $Q/2\pi r\nu$, were comparable (around 5 or 10) in the two investigations.

The cause of these stationary dye sheets has not yet been established. Although it is less likely than in the work of Arons *et al* (who worked with a free upper surface) that they were due to spurious thermal effects, this possibility has not yet been eliminated. Temperature variations of 10^{-2} or 10^{-3} centigrade degrees within the fluid can be very troublesome when investigating details of the very slow flows.

If it turns out that the dye sheets were not due to spurious thermal effects, then it will be necessary to entertain the possibility that vertical motions in the Ekman layers, caused by local axisymmetric instabilities or by the interaction of the side-wall boundary layers or the interior region with the Ekman layers (see Stern 1960), might have been responsible. (The Ekman layer instabilities reported by Gregory, Stuart & Walker (1955), Faller (1963) and Tatro & Mollo-Christensen (1967), who worked at much higher Reynolds numbers than in the present experiments, are not axisymmetric and give rise to travelling—not stationary—disturbances.)

Very complicated instabilities can occur when the basic flow is non-axisymmetric. Figure 13*c* shows that one effect of reducing Ω by a large factor (and simultaneously increasing Q by a small factor) on the laminar flow illustrated by figure 7*b* is the production of several intense vortices superimposed on, and advected with, a general flow pattern that otherwise remains qualitatively unaltered.

8. Experiments with containers of non-uniform depth ($\nabla_1 D \neq 0$)

We conclude this paper with a brief discussion of a few examples of source–sink flows in containers for which the depth variations are so much larger than the Ekman-layer thickness that, in contrast to the flows discussed in §7, end effects result almost entirely from the *non*-viscous contribution to the right-hand side of (4.6). When the Rossby and Ekman numbers (see (5.7) and (6.1)) tend to zero, the flow is geostrophic and the left-hand side of (4.6) also tends to zero. Hence $\bar{\mathbf{u}} \cdot \nabla_1 D(x, y) \doteq 0$, implying that the trajectories of each fluid filament must be such that D remains constant along it. In all examples considered, z_u is constant and z_l depends only on r; hence, geostrophic streamlines are circles concentric with the z-axis.

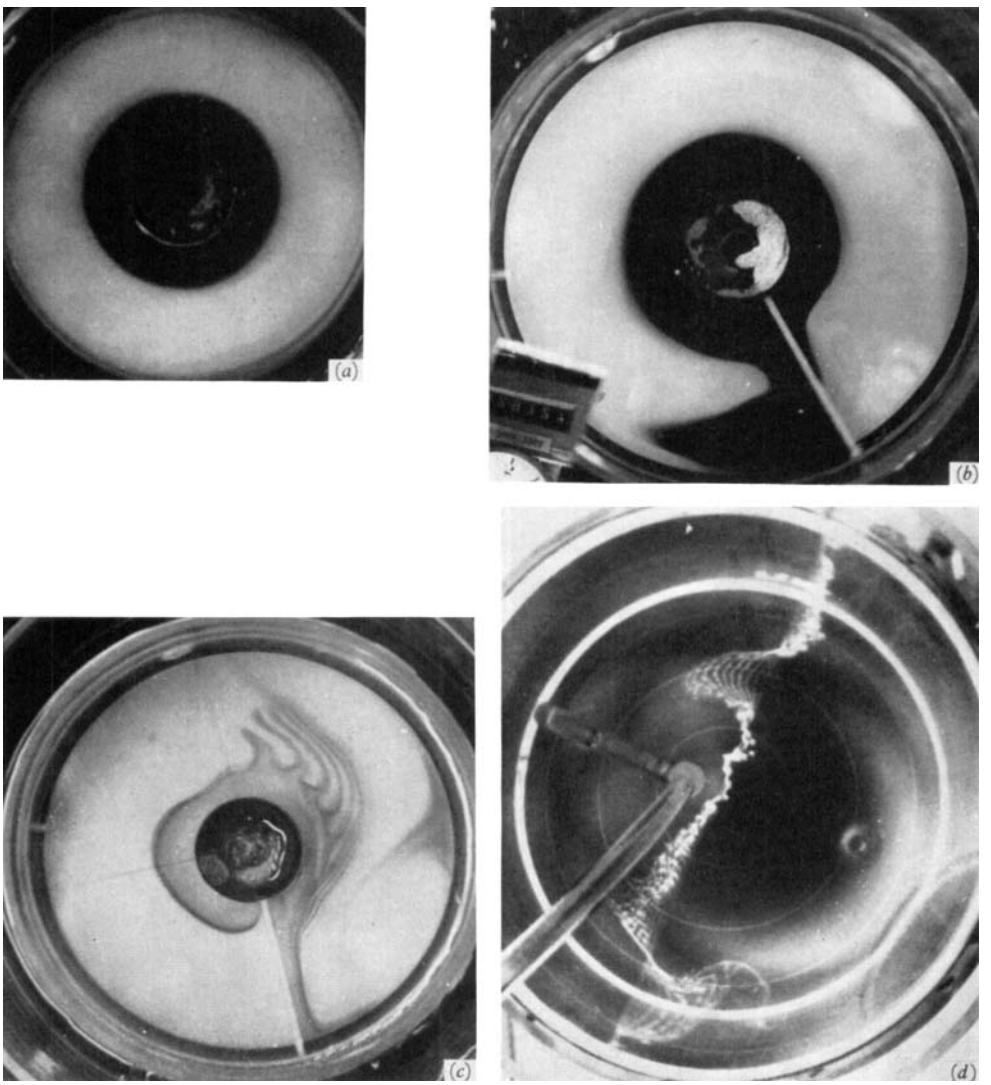

FIGURE 12. The effects of non-uniform depth on two flows for which $j \neq 0$ ((*a*) and (*d*), cf. figures 7*a* and 8*c*) and on one flow for which $j = 0$ ((*b*) and (*c*), cf. figure 6*a*). (*a*), (*b*) and (*c*) show the distribution of nigrosine dye several minutes after it had been introduced at the surface of the source. (*d*) shows the effects of the flow on lines of dye released from a wire stretched along a diameter at 90° to the plane passing through the axes of the source and the sink.

(*a*), where the bottom slope is positive (i.e. $dD/dr < 0$), should be compared with figure 10*e*, for which Q and Ω are the same and $\bar{D}$ nearly the same but $dD/dr = 0$. Although the two flows are basically similar, the sloping bottom evidently inhibited any tendency for non-axisymmetric instabilities to occur.

(*b*) and (*c*) illustrate flows under conditions that are comparable in every respect except for opposite (but equal) bottom slopes; $dD/dr > 0$ for (*b*), $dD/dr < 0$ for (*c*). The sloping bottom produces zonal relative motion which is not present in figure 6*a*, for which D is uniform. A boundary layer occurs on one side of the radial barrier; the sense of the zonal motion and the position of the boundary layer depend on the sign of the slope.

(*d*) shows how a (negative) bottom slope modifies the flow so strongly that in contrast to the gyres illustrated by figures 7*c* and 8, its direction is mainly zonal. Had the bottom slope been zero, the dye released at the wire would have remained close to the wire until diffusion effects became noticeable (see § 8, cf. figure 8*c*). (See table 1 for experimental details.)

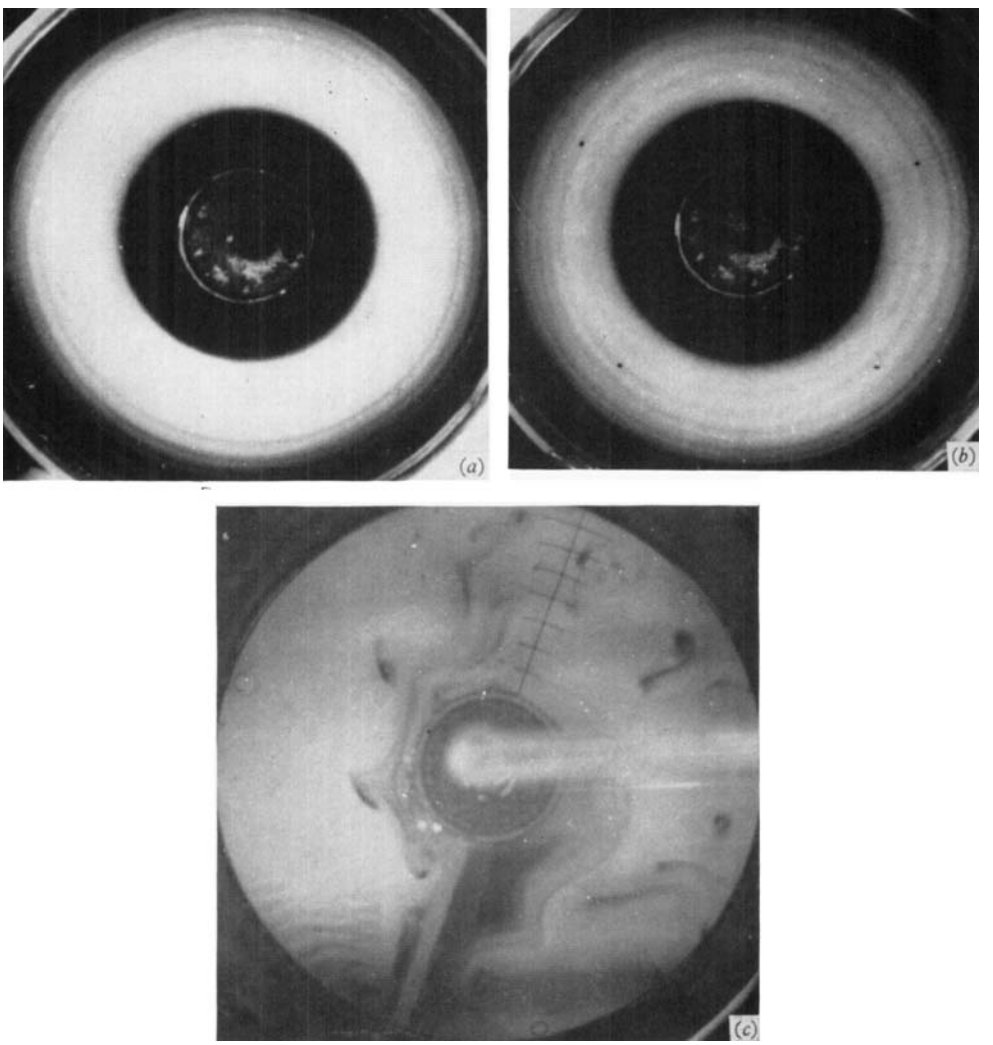

FIGURE 13. Further examples of instabilities (cf. figures 10*e*, *f* and 12*c*). Figures 12*a*, 13*a* and *b* are three photographs of the same flow taken 4, 10 and 20 min after the commencement of a continuous injection of dye via the surface of the source. Note the presence in the interior region of faint dye sheets (seen end on); these sheets may be manifestations of some form of axisymmetric instability (see text).

(*c*) shows that one effect on the laminar flow illustrated by figure 7*b* of reducing Ω by a large factor (and simultaneously increasing Q by a small factor) is the production of several intense vortices superimposed on, and advected with, a general flow pattern that otherwise remains qualitatively unaltered. The Ekman and Rossby numbers (γ and ϵ, see (5.7) and (6.1)), were, respectively, 10^{-2} and 1 approximately for this experiment, and very much greater than the corresponding values of γ and ϵ for the other experiments. (See table 1 for full experimental details.)

Case (i): $j = 0$ (cf. §7)

Figures 12*b* and *c* illustrate flows under conditions that are comparable to each other in every respect except for opposite (but equal) bottom slopes, negative for (*c*) and positive for (*b*) (see table 1, cf. figure 6*a*; see Stommel, Arons & Faller (1958) and Faller (1960) for related work). The sloping bottom produces zonal relative motion, which in turn gives rise to a boundary layer on one side of the radial barrier, in which much of the radial transfer of fluid occurs. The general sense of the zonal motion and the position of the boundary layer depend on the sign of the slope. Thus, for example, in accordance with (4.6), when $dz_l/dr > 0$ (cf. figure 12*b*), a fluid filament develops a strong positive axial vorticity, ζ, and swings 'eastward' as it moves outward from the source. It eventually joins the boundary layer on the 'western' side of the radial barrier and then continues to move radially outward, with little or no azimuthal component of motion. On leaving the boundary layer on the barrier, the filament swings 'westward' into a boundary layer on the sink from which it finally leaves the system.

When $dz_l/dr < 0$ (see figure 12*c*), the zonal motion is opposite to that described above for the case $dz_l/dr > 0$ (see figure 12*b*), and the viscous boundary layer on the radial wall now occurs on its 'eastern', rather than its 'western', side. Further work will be needed to establish why the irregular features seen in the first quadrant of figure 12*c* are not present in figure 12*b*.

Case (ii): $j \neq 0$

Comparison of figure 12*a* (see also figures 13*a* and 13*b*), for which D is variable, with figure 7*a*, for which D is uniform, shows that, in contrast to cases where $j = 0$ (see figure 3, cf. figure 2) such as the one just considered, when $j \neq 0$ and the flow is axisymmetric the flow is not profoundly affected by an axisymmetric sloping bottom (although, as noted in §7, one effect of the sloping bottom seems to be the suppression or inhibition of non-axisymmetric instabilities (cf. figure 10*e*)). It should be a straightforward matter to extend the theory of the side-wall boundary layers developed in §5 to cases where D is no longer uniform, and to carry out related experimental studies of the structure of these boundary layers, along the lines of the experiments described in §7 above.

In conclusion mention should be made of the complicated experiment that led to all the others discussed in this paper. In that experiment, illustrated by figure 12*d*, the profound effect of an axisymmetric sloping bottom on non-axisymmetric source–sink flows (with $j = 2$, see figure 3*c*) was investigated briefly. Had the bottom slope been zero, as in figures 7*c* and 8, the motion in the main body of the fluid would have comprised two gyres, one surrounding the source and the other surrounding the sink, with a plane of symmetry on which $\mathbf{u}$ has no zonal component passing through the axis of the container at right angles to the plane containing the axes of the source and sink.

Such a flow pattern is not consistent with $\bar{\mathbf{u}} \cdot \nabla_1 D \doteq 0$ when $\nabla_1 D \neq 0$. An axisymmetric bottom slope gives rise to a motion that is mainly zonal everywhere, as dye released from a wire placed in the plane of symmetry mentioned above clearly indicates (see figure 12*d*). The zonal motion at distances from the axis of the container close to that of the source and sink appeared to be directed *towards*

the source, suggesting that, as in the case of zero bottom slope, much, if not all, of the transport of fluid from source to sink took place via boundary layers, and not via the main body of the fluid. Further work is clearly needed here.

The work of the Geophysical Fluid Dynamics Laboratory, Department of Geology and Geophysics, M.I.T., is supported by the National Science Foundation (Atmospheric Sciences Program); this is paper number 22 of that laboratory.

Appendix. Steady two-dimensional axisymmetric flows

The simplest conceivable flow in a system for which $j \neq 0$ (see (3.14)–(3.19)) is the axisymmetric motion that arises when the source and sink are coaxial porous rigid cylinders in $r = a$ and $r = b$ (i.e. $m = 2$, $g_1(x, y) = (x^2+y^2-a^2)$, $g_2(x, y) = (x^2+y^2-b^2)$) and $f(P)$ is independent not only of z but also of the azimuthal angle θ (see figure 3a). Fluid enters and leaves at the constant rate $q/2\pi$ cubic centimetres per second per unit length in the z direction per unit angular distance in the azimuthal direction (see (3.1) and figure 3a). The theory of this flow was first discussed by Hamel (1916).

Exact solutions of (3.5) to (3.10) under the appropriate boundary conditions, namely $r\partial\phi/\partial r = q/2\pi$ and $\partial A/\partial r = 0$ on $r = a$ and $r = b$, are the following:

$$\partial\phi/\partial r = q/2\pi r, \quad \partial p/\partial\theta = 0,$$

$$\frac{\partial A}{\partial r} = \Omega\left[-r + \frac{1}{b^{S+2}-a^{S+2}}\left\{\frac{b^2a^2(b^S-a^S)}{r} + (b^2-a^2)\,r^{S+1}\right\}\right], \tag{A 1}$$

$$\frac{1}{r}\frac{\partial}{\partial r}\left(r\frac{\partial A}{\partial r}\right) = \zeta = 2\Omega\left\{(1+\tfrac{1}{2}S)\left[\frac{(b^2-a^2)\,r^S}{b^{S+2}-a^{S+2}}\right] - 1\right\}; \tag{A 2}$$

the dependence of $\partial A/\partial r$ on r and S is illustrated by figure (A 1). Here

$$S \equiv Rq/|q|, \quad R \equiv |q|/2\pi\nu, \tag{A 3}$$

q being reckoned positive or negative according as the source–sink flow is directed radially outwards or inwards; R is a Reynolds number based on the source strength.

The result that $\partial\phi/\partial r$ is independent of R is not, of course, surprising, since the radial motion is determined entirely by continuity considerations. When $R \gg 1$ and $q > 0$,

$$\frac{\partial A}{\partial r} = \Omega\left\{\frac{(b^2-a^2)}{b}\left(\frac{r}{b}\right)^R + \frac{a^2}{r} - r\right\},$$

$$\frac{1}{r}\frac{\partial}{\partial r}\left(r\frac{\partial A}{\partial r}\right) = \zeta = -2\Omega\left\{1 - \tfrac{1}{2}R\left(1-\frac{a^2}{b^2}\right)\left(\frac{r}{b}\right)^R\right\}, \tag{A 4}$$

with comparable but slightly different expressions when $q < 0$. According to (A 4), except in the vicinity of the sink, where a viscous boundary layer of thickness b/R (or a/R when $q < 0$) occurs, individual fluid particles conserve their angular momentum and the azimuthal flow has zero absolute vorticity (cf. 3.18). Within the boundary layer on the sink, where $b(1-R^{-1}) \leqslant r \leqslant b$,

$$\frac{\partial A}{\partial r} = -\Omega R\left(1-\frac{a^2}{b^2}\right)(b-r),$$

$$\frac{1}{r}\frac{\partial}{\partial r}\left(r\frac{\partial A}{\partial r}\right) = \zeta = \Omega R\left(\frac{b^2}{a^2}-1\right). \tag{A 5}$$

In the inviscid limit ($R \to \infty$) the no-slip condition is no longer satisfied on the sink.

The other limit, $R \ll 1$, is also interesting (see figure A 1); then, by (A 1) and (A 2),

$$\frac{\partial A}{\partial r} = \Omega b R\left\{\left[\frac{\ln(b/a)}{b^2/a^2-1}\right]\left[\frac{b}{r}-\frac{r}{b}\right]-\frac{r}{b}\ln\frac{b}{r}\right\},$$

$$\frac{1}{r}\frac{\partial}{\partial r}\left(r\frac{\partial A}{\partial r}\right) = \zeta = 2\Omega R\left\{\left[\frac{1}{R}+\left(\frac{1}{2}-\frac{(\ln(b/a)}{(1-a^2/b^2)}\right)\right]\left(\frac{r}{a}\right)^R-\frac{1}{R}\right\}. \tag{A 6}$$

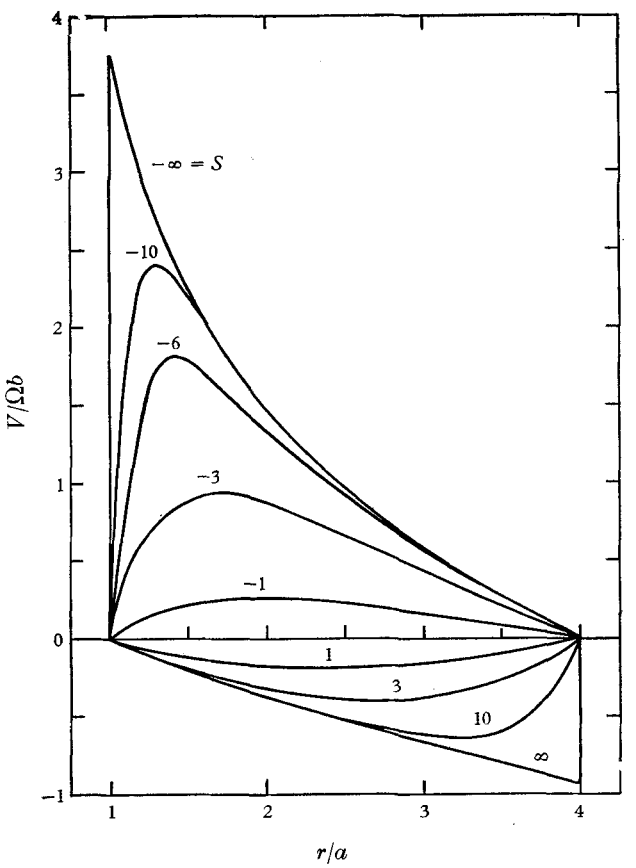

FIGURE A 1. The variation of azimuthal velocity V with r for an annular system when $b/a = 4$ at different values of $S \equiv q/2\pi\nu$ (see figure 3a and equation (A 1)). When $|S| \gg 1$ individual fluid particles tend to conserve their angular momentum in the main body of the fluid, the corresponding relative vorticity, ζ, being close to -2Ω. A boundary layer, of thickness b/S when $S > 0$ (and $a/|S|$ when $S < 0$), and in which $\zeta \sim |S|\Omega$, forms on the surface of the sink, but there is no corresponding boundary layer on the source.

The simplest conceivable flow in a system for which $j = 0$ is the motion that arises when the annular source–sink arrangement (see figure 3a) is modified by connecting the two bounding cylinders in $r = a$ and $r = b$ by a thin, rigid, impermeable barrier (see figure 2a). This modification changes m from 2 to 1 and leads to the automatic satisfaction of (3.16) (cf. figure 2d).

The flow is no longer strictly axisymmetric; when $\nu \neq 0$, $\partial\phi/\partial r$ cannot be independent of θ and at the same time satisfy the 'no-slip' condition on the radial barrier. Moreover, owing to the presence of the barrier, $\partial p/\partial\theta$ need not vanish (cf. (A 1)). In the inviscid limit, however,

$$\frac{\partial\phi}{\partial r} = \frac{q}{2\pi r}, \quad \frac{\partial A}{\partial r} = 0, \quad \frac{\partial p}{\partial\theta} = \frac{\Omega q}{\pi}, \tag{A 7}$$

are exact solutions of (3.5)–(3.10) (cf. (3.19) and (A 1)–(A 4)). The relative flow then has neither circulation nor vorticity, the only effect of Ω being the setting up of an azimuthal pressure gradient supported by the barrier. This pressure gradient (cf. (3.14)) supplies the torque required to change the energy and the angular momentum of a fluid particle as it moves radially without suffering any sideways displacement. The jump in p across the barrier, $2\Omega q$, exactly offsets the Coriolis acceleration associated with the radial flow.

It might be of interest to conclude by mentioning that the effect of rotation on two-dimensional source–sink flows is roughly analogous to that of a magnetic field on electric currents in a fixed conductor (Hall effect). The analogues of $j = 0$ systems (see figure 2) arise when the shape of the conductor is such that a permanent electric charge distribution can be set up to provide an electric field (analogous to $\nabla_1 p$) that exactly offsets the effect of the magnetic field (analogous to $\boldsymbol{\Omega}$) on the electric current (analogous to $\mathbf{u}$); the electric current flow will then be unaffected by the magnetic field, whose effect is manifested as a 'Hall potential'. When, owing to the shape of the conductor, no such charge distribution can be set up we have the analogues of $j \neq 0$ systems (see figure 3); the magnetic field then gives rise to a 'Hall current'.

REFERENCES

Arons, A. B., Ingersoll, A. P. & Green, T. 1961 *Tellus*, **13**, 31.

Barcilon, V. 1967 *J. Fluid Mech.* **27**, 551.

Charney, J. G. & Eliassen, A. 1949 *Tellus*, **1**, no. 2, 38.

Faller, A. J. 1960 *Tellus*, **12**, 159.

Faller, A. J. 1963 *J. Fluid Mech.* **15**, 560.

Gregory, N., Stuart, J. T. & Walker, W. S. 1955 *Phil. Trans. Roy. Soc. Lond.* A **248**, 155.

Hamel, R. 1916 *Jahrs. deutschen Math. Ver.* **25**, 34.

Herbert, D. M. 1965 *J. Fluid Mech.* **23**, 65.

Hide, R. 1963 *Mém. Soc. Roy. Sci. Liège*, V **7**, 481.

Hide, R. 1966 *Bull. Am. Meteorol. Soc.* **47**, 873.

Hide, R. 1967 *Phys. Fluids*, **10**, S 306.

Hide, R., Ibbetson, A. & Lighthill, M. J. 1968 *J. Fluid Mech.* **32**, 251.

Lamb, H. 1945 *Hydrodynamics*. New York: Dover.

Lewellen, W. S. 1965 *Am. Inst. Aero. Astro. J.* **3**, 91.

Prandtl, L. 1952 *Essentials of Fluid Dynamics*. London: Blackie and Sons.

Proudman, I. 1956 *J. Fluid Mech.* **1**, 505.

Proudman, J. 1916 *Proc. Roy. Soc. Lond.* A **92**, 408.

Rott, N. & Lewellen, W. S. 1966 Article in *Progress in Aeronautical Sciences*, **7** (ed. D. Küchemann). Oxford: Pergamon Press.

Stern, M. E. 1960 *Tellus*, **12**, 399.

Stewartson, K. 1957 *J. Fluid Mech.* **3**, 17.

Stommel, H., Arons, A. B. & Faller, A. J. 1958 *Tellus*, **10**, 179.

Tatro, P. R. & Mollo-Christensen, E. L. 1967 *J. Fluid Mech.* **28**, 531.

Taylor, G. I. 1917 *Proc. Roy. Soc. Lond.* A **93**, 99.